Contrast Mechanisms for Tumor Imaging at 0.35T

By

Niloufar Zakariaei

A dissertation/thesis submitted in partial fulfillment of
the requirements for the degree of

Master of Science

Wayne State University
Department of Biomedical Engineering

July 2019

To the Faculty of Wayne State University:

The members of the Committee appointed to examine the dissertation/thesis of Niloufar Zakariaei find it satisfactory and recommend that it be accepted.

_____

Ewart Mark Haacke, Ph.D., Chair

_____

Carri Glide-Hurst, Ph.D.

_____

Yu-Chung Cheng, Ph.D.

_____

Zhifeng Kou, Ph.D.

Note

This is an abridged version of my thesis, results of patient images were deliberately omitted according to Henry Ford Health System (HFHS) code on protecting patient information.

For more information please contact me at:

niloufar.zakariaei@wayne.edue

Dedication

To my uncle Alireza who is

a rare mixture of ingenuity, gravity and gentility.

Acknowledgments

“Ever tried, ever failed, no matter! Try again, fail again, FAIL BETTER”

Ultimately, this journey has ended up. This chapter of life was arduous, yet noteworthy. Foremost, I would like to express my sincere gratitude to my sublime advisor Prof Ewart Mark Haacke who gave me the opportunity to come to the United States and be present at the graduate school. I have been motivated by his continuous support, patience, enthusiasm and intimate knowledge to fulfil my master study and research. Up to end of my academic career, working with him is my educational honor.

My sincere thanks dedicate to my co-adviser Dr. Carri Glide-Hurst and her professional team at Henry Ford health system. I got a chance to go beyond academic circumstance and discover state of art applications of my research in practice and all of this path because of my luck to work with her. A pivotal character who exhibits that carrying out research and clinic simultaneously is possible.

My special thanks go to Dr. Siamak Nejad Daravani. My main background was magnetic resonance imaging (MRI) ; however, my thesis focused on combination of MRI in radiation therapy (RT). I could not have imagined having a better mentor than Dr. Nejad to fill this gap. His passion to instruct every required elements and modest characteristic was exemplary for me.

Beside my advisors, I would like to thank the rest of my thesis committee: Dr. Cheng and Dr. Kou for their encouragement, insightful comments and deep questions.

Last but not least, I want to say thanks to role models; my mom and dad whose supports surpass frontiers. They taught me that we should be daring enough to follow our hearts and dreams. They are most prestigious asset in my life. My uncle’s presence in the US was such heart warning that I was capable to overcome all the difficulties. His ingenuity, benignity, creativity is always inspiring for me. He is supportive enough to eliminate my lonesome feeling for being away from family.

Table of Contents

Page

List of Figures

Page

List of Tables

Page

Abbreviations

2D 2-dimension

3D 3-dimension

ART Adaptive Radiation Therapy

bSSFP balanced Steady State Free Precession

CSF Cerebrum Spinal Fluid

CT Computed Tomography

CNR Contrast-to-Noise Ratio

EPI Echo Planer Imaging

FA Flip Angle

FLASH Fast Low Angle SHot

GM Gray Matter

GRE Gradient Recalled Echo

GTV Gross Tumor Volume

ICR Intracranial Relapse

IMRT Intensity Modulated Radiotherapy

IR Inversion Recovery

ISMRM International Society of Magnetic Resonance in Medicine

Linac Linear Accelerator

MR Magnetic Resonance

MRI Magnetic Resonance Imaging

MRgRT Magnetic Resonance-Guided Radiation Therapy

NIST National Institute of Standards and Technology

NMR Nuclear Magnetic Resonance

OS Overall Survival

PD Proton Density

qMRI Quantitative Magnetic Resonance Imaging

RF Radio Frequency

ROI Region of Interest

RT Radiation Therapy

SE Spin Echo

SNR Signal-to-Noise Ratio

STAGE STrategically acquired gradient echo

TE Echo Time

TR Repetition Time

VFA Variable Flip Angle

WM White Matter

$IGRT_x$ X-ray-Based Image-Guided Radiation Therapy

Abstract

Cancer is a challenging public health problem worldwide and the second leading cause of death in the United States. One in four deaths in the United States is because of cancer. In particular, it is estimated that 1/3 of all brain tumors are malignant and approximately 26000 new malignant brain tumor cases detected in 2019. Glioblastoma multiforme (GBM) is recognized as the most dominant and fatal primary brain malignancy among all brain tumors.

Radiation therapy (RT) is a crucial approach to cancer treatment and has been found to influence the cure or palliation of numerous cancer types. It's estimated that 52.3% of all cancer patients have been in exposed to RT. Technology advances have culminated in the cutting-edge technique named Intensity modulated radiotherapy (IMRT), which can effectively allow dose to be concentrated in the tumor volume while sparing normal tissues.

Magnetic resonance-guided radiation therapy (MRgRT) has shown great promise for localization and real-time tumor tracking; however, limited work has been done in studying tumor response at low magnetic field strengths. The ViewRay MRIdian linac® system is an integrated MRgRT instrument designed to render MR images and range of external-beam RT options simultaneously. The range can be varied from basic fields to complete on-couch adaptive and MR-controlled IMRT at the same isocenter.

Our site uses a Siemens 0.35T scanner coupled with the MRIdian Linac (ViewRay, Mountain View, CA) linear accelerator to map out tumors for radiation planning. Part of any planning tool is to have multiple contrasts and quantitative mapping to best delineate the boundaries and characteristics of the tumor.

Here we optimize strategically acquired gradient echo (STAGE) imaging for a 0.35T MR-linear accelerator to yield 4 qualitative (T1-weighted, enhanced T1-weighted, proton-density (PD), and FLAIR), and 4 quantitative (T1 maps, PD maps, susceptibility weighted imaging (SWI), and R2* maps) datasets. We then validate the T1, PD and $R2^*$ map values at 0.35T to benchmark our results using an ISMRM\NIST phantom.

Chapter 1

Thesis Motivation

and

Outline

1.1 Introduction

Cancer is a challenging public health problem worldwide and the second leading cause of death in the United States (Siegel, Miller, & Jemal, 2019). One in four deaths in the United States is because of cancer (Siegel et al., 2019). Radiation therapy (RT) is a crucial approach of cancer treatment and has been found to influence the cure or palliation of numerous cancer types. It's estimated that 52.3% of all cancer patients have been in exposed of RT (Delaney, Jacob, Featherstone, & Barton, 2005). While the purpose of radiation is to maximize control over tumors, it targets cancerous cells and surrounding healthy tissues at the same time.

Advances in technology have culminated in the cutting-edge technique named intensity modulated radiotherapy (IMRT), which can effectively allow doses to be concentrated in the tumor volume while sparing normal tissues (Macklis, 2006). This is a substantial step forward, especially for children in whom sparing normal tissue to preclude long-term consequences is significantly important. However, the full exploitation of the corrected-forming potential absolutely required reliable detailed data of the patient's anatomy at the time of treatment (Oelfke, 2015).

To solve this involved problem, a hybrid technology that consisted of a kilo-voltage X-ray source and a flat panel imager with cutting-edge dose delivery equipment were developed as X-ray-based image-guided radiation therapy ($IGRT_x$) (Oelfke, 2015). The technology has been widely accessible for clinics for over a decade; however, two intrinsic flaws accompany it:

First, $IGRT_x$ suffers from poor contrast, making it impossible to distinguish a tumor from adjacent healthy tissues. Second, adaptive and continuous monitoring of intrafraction organ motion is baffling. Acquisition time for 3 dimension (3D) is not clinically feasible. Continuous X-ray imaging can deliver reasonable contrast with an unacceptable accumulation of imaging doses (Oelfke, 2015).

Magnetic resonance-guided radiation therapy (MRgRT) provides superior image guidance for radiotherapy treatments in comparison to conventional computed tomography (CT). The excellent soft tissue contrast of magnetic resonance (MR) empowers strong tissue distinction to visualize the gross tumor volume (GTV) and surrounding tissues in the treatment of abdominal and thoracic malignancies. Figure

1 compares the same cross section imaged by CT (a) and MR (b) to show the potential ability to identify GTV. Real-time, accurate inter/intrafraction localization and tumor tracking integrated with advanced motion correction algorithms are notable adaptive capabilities in MR (Mittauer et al., 2018).

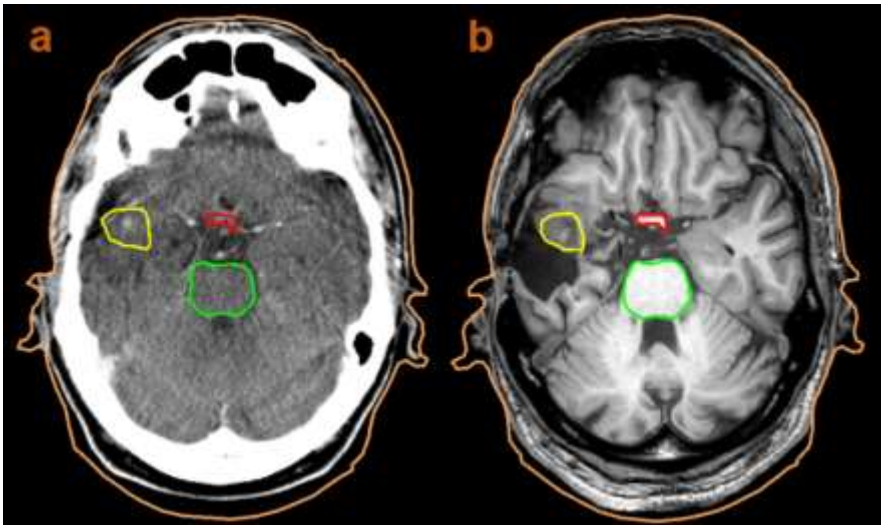

Figure 1. Comparison of visualization of GTV in CT and MR image. a) CT slice and b) T1 3D Turbo Field Echo (TFE) MR slice. Orange contour, green, yellow and red displays of the human head, brainstem, tumor and optic chiasm, respectively.[1]

However, designing a hybrid technology integrating magnetic resonance imaging (MRI) scanner with a linear accelerator (linac) was formidable because of two challenges. First, “electromagnetic decoupling” technology was required to dissociate the strong magnetic field of MRI from the dose delivery system (Oelfke, 2015). The interference of the magnetic field and linac may corrupt the image quality. Second, a new guideline was required for dose distribution because it would be affected by extra Lorentz force operation on every dose-deposition electron moving in the static magnetic field of the scanner (Oelfke, 2015). In particular, new dosimetry protocols, dose calculation algorithms and treatment planning had to be established. Specifically, development of MRgRT required allocated calibration and quality assurance to warrant geometrical accuracy.

The issues started to be addressed by University Medical Center (UMC) at Utrecht and University of Florida (UoF) a decade ago. The device produced at UoF is the commercially accessible MRIdian system (ViewRay, United States) (Oelfke, 2015). It

[1] The image is adapted from “Towards real-time plan adaptation for MRI-guided radiotherapy”, PhD Thesis, Utrecht University, The Netherlands

accomplished the ‘electromagnetic decoupling’ of the MRI scanner and dose delivery system by substituting the linac with three ^{60}Co sources (Mutic & Dempsey, 2014). However, the new combination requires using a split magnet, which resulted in a compromise of a relatively low magnetic field of 0.35T for MRI. Early results of patient treatments were conducted in January 2014.

1.2 The ViewRay System

The ViewRay MRIdian linac® system is an integrated magnetic resonance-guided radiation therapy (MRgRT) instrument designed to render MR images and range of external-beam RT options simultaneously. The range can be varied from basic fields to complete on-couch adaptive and MR-controlled intensity modulated RT (IMRT) at the same isocenter. The device consists of 3 main parts (Mutic & Dempsey, 2014):

1- The MRI: It consists of a vertical space (double donut) with horizontal solenoidal superconducting 0.35T entire body MRI. The vertical gap in the main magnet is overlapped with the 50 cm diameter spherical imaging field of view. Gradient coils are self-shielded; they are thrust and torque compensated to lessen loads and noise. The split gradient coil has an inner diameter of 80 cm with a thin, cylindrical, inner former connecting the halves across a 20 cm central section where no winding or electrical connection are present. Entire connections and cooling channels are emanated from the outer terminal of the coils. The upper bound for the maximum gradient strength and slew rate is 18 mT/m and 200 T/m/s on each axis, respectively. The whole-body radio frequency (RF) transmit coil is a 75 cm diameter, 16-rung quadrature birdcage coil with capacitance disturbed along the end rings and the rungs. Manufacturers integrated the RF-shield with the whole-body RF transmit coil to make a modular coil or shielded unites to span the magnetic gap, yet it is thin and uniformly attenuated to preclude beam heterogeneities. Surface MRI array coils are thin and covered with light foam to minimize surface dose and increase patient comfort. In addition, they are uniformly attenuated with approximately 0.75% beam attenuation (Figure 2 a)

2- The RT delivery system: It is a robotic 3-headed ^{60}Co system which supplies a dose rate of 550 cGy/min from three 10.5*10.5 cm^2 fields to the isocenter at installation, paired with a quick, pneumatic and source-strobing mechanism.

Generally, 3 sources can prepare the dose rate at the same level as conventional accelerators in addition to synchronous delivery from 3 gantries separated with 120° angles. The VRS layout empowers axial radiation to patients with minimal attenuation. Figure 2 a) shows a schematic configuration revealing the location of the RT gantry iso-center in the center of the main scanner. During usage, the instrument track targets the desired structures which can be observed in fast, continuous and simultaneous planer images, in 1 sagittal plane at 4 frames per second or in 3 parallel sagittal planes at 2 frames per second. The real time images with registration-based beam control enable region of interest (ROI) tracking with a determined boundary with approximately 300 ms latency.

3- The adaptive RT (ART) treatment planning system: This section has three components including high-performance computing planning and delivery software that enables auto contouring, a priori Monte Carlo dose computation and IMRT or conformal RT planning or both utilized to reinforce 3D conformal RT, IMRT and on-couch ART. The treatment planning system is fast enough to provide ART treatments based on volumetric images of the day. It can do 9 field plans with complete optimization, and lead motion calculation and dose calculation in less than 30s. Figure 3 demonstrates screen captures from the adaptive planning work flow.

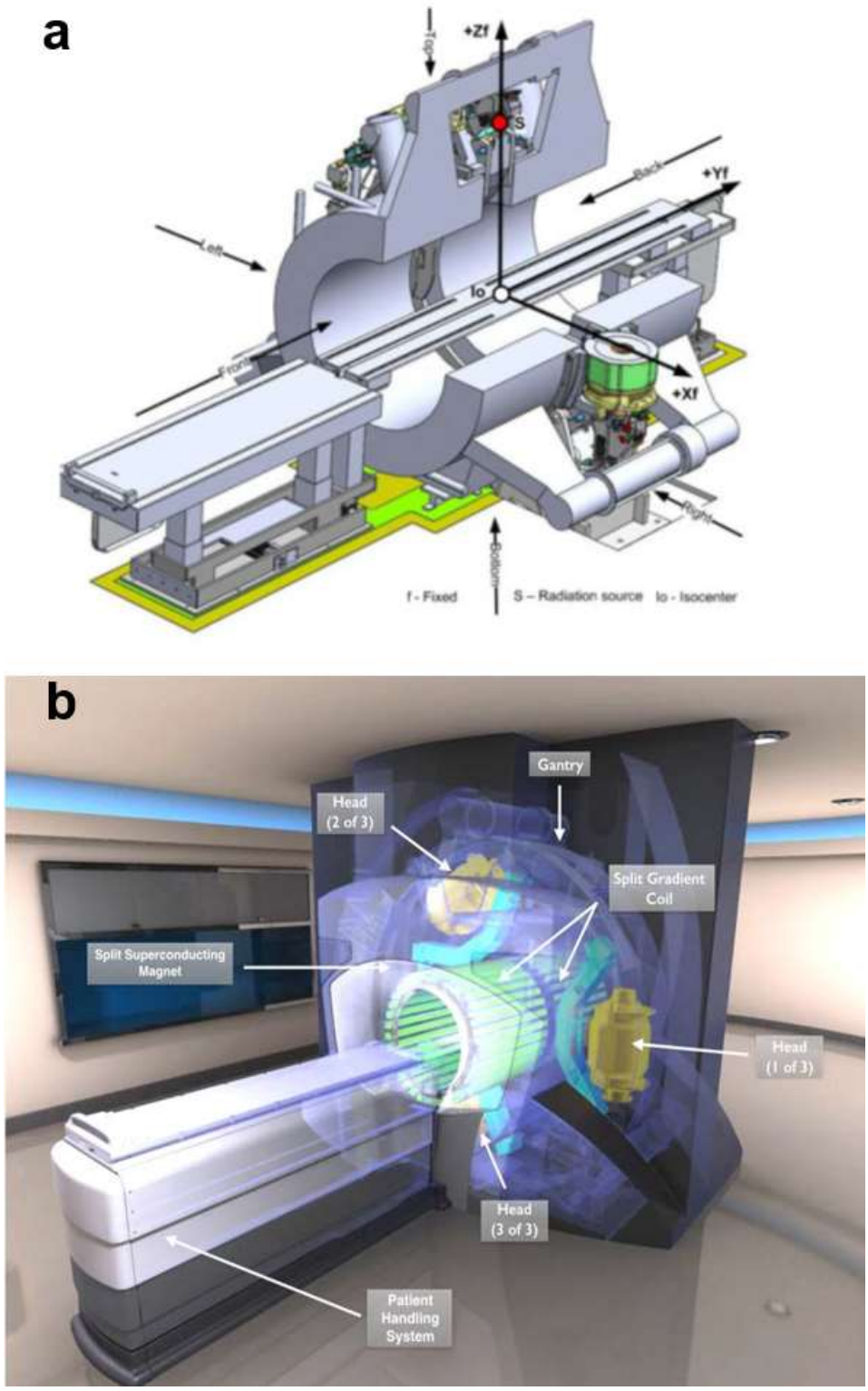

Figure 2 . ***a)*** *. A view of the ViewRay system exposing the quadrant of the MRI bore through 28 cm gap and half of the radiation therapy head at 90˚,* ***b)*** *A schematic of the integration of the main parts of the ViewRay system*

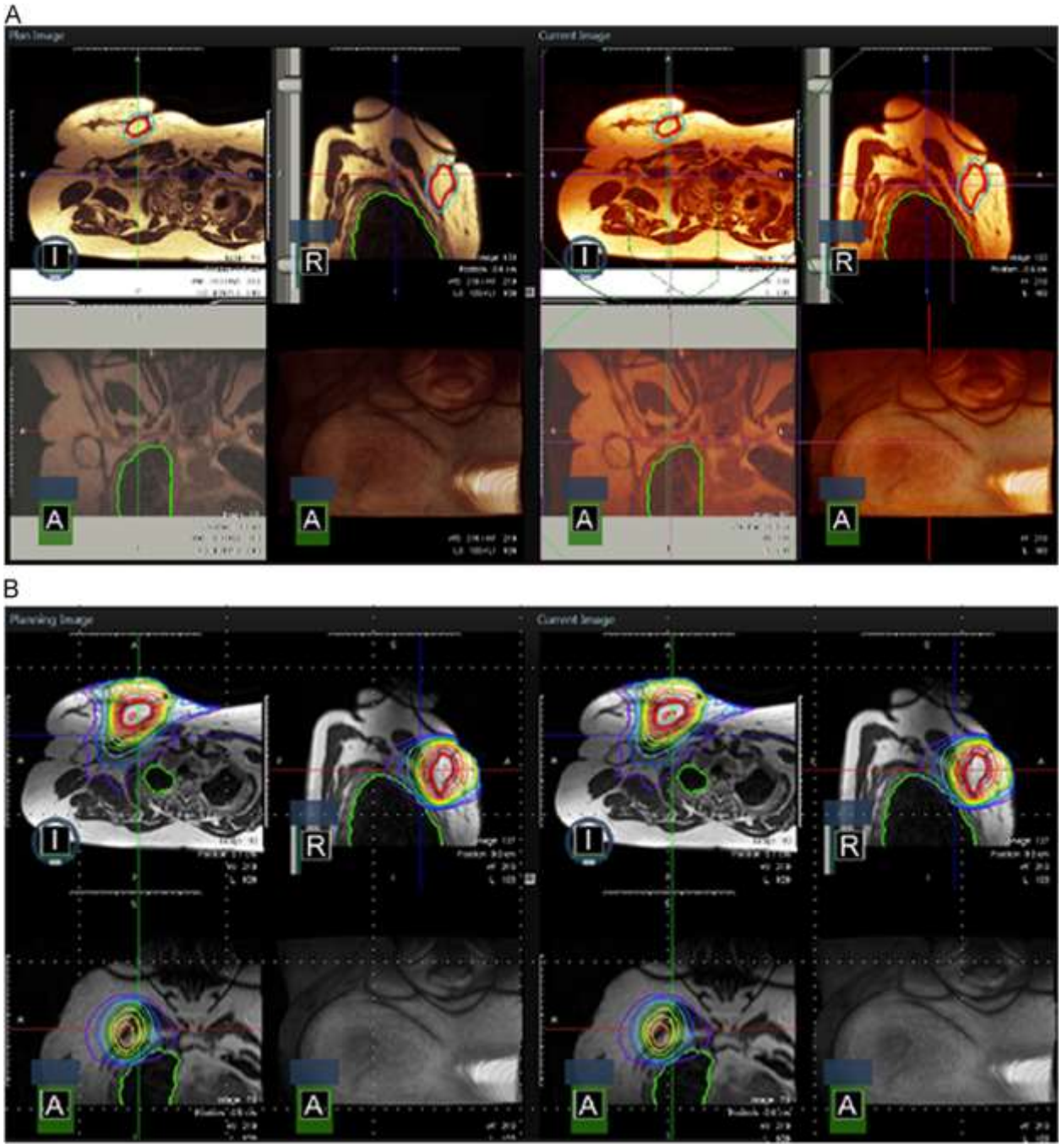

Figure 3. ***A)*** *A screen capture of a patient with breast cancer in the ViewRay system (left, original and right, daily treatment). The patient is undergoing treatment with accelerated partial-breast irradiation, and the screen capture indicates a daily MR images* ***B)*** *A corresponding auto-contoured and reoptimized IMRT treatment plan of the images in part (A)*[2]

[2] The image was adapted from "The ViewRay System: Magnetic Resonance-Guided and Controlled Radiotherapy". *Seminars in Radiation Oncology*, *24*(3), 196–199. https://doi.org/10.1016/j.semradonc.2014.02.008

1.3 Thesis Outline

It is estimated that 1/3 of all brain tumors are malignant, with approximately 26000 new malignant brain tumor cases likely to be detected in 2019 (Society, N.B.T, 2019). Glioblastoma multiforme (GBM) is recognized as the most dominant and fatal primary brain malignancy among all brain tumors (Sulman et al., 2017). Although surgical and adjuvant therapies have progressed, statistics show that the median survival of GBM less than 2 years, which indicates how extremely aggressive at GBM tumor is (Han et al., 2015). It has been observed that increasing the radiation dose to the tumor sub-volume locally may ameliorate intracranial relapse (ICR) and overall survival (OS) (Zschaeck et al., 2018). However, tumor sub-volume texture demonstrates variations in post-surgical states as observed by diagnostic MRI at 1-2 time points over an RT course (Tsien et al., 2005); (Yang et al., 2016); (Shukla et al., 2017). The changes emerged as surgical cavity and gross tumor volume decreased, inferring that changes to the RT course may potentially save healthy brain tissue.

In a study with 3 patients, MRgRT TrueFISP serial datasets exhibited changes in the resection cavity, cerebral edema and tumor volume during the RT course (Malmstrom et al., 2012), indicating agreement with our experiment.

It is perceived that geometrical changes occurred in a small region of the brains during treatment based on limited time points. However, (1) the effect of qMRI using MRgRT to discern the tumor response index over of the course of treatment and (2) the probability of the effectiveness of MR-guided ART to reduce overall healthy brain and normal organ at risk doses in response to changing anatomy are questionable.

Our site uses a Siemens 0.35T scanner coupled with the MRIdian Linac (ViewRay, Mountain View, CA) linear accelerator to map tumors for radiation planning. Part of any planning tool is to have multiple contrasts and quantitative mapping to best delineate the boundaries and characteristics of the tumor. We propose to create new contrast mechanisms for imaging tumors at 0.35T using strategically acquired gradient echo (STAGE) imaging. STAGE provides a set of qualitative and quantitative images for tissue evaluation. More specifically, STAGE provides quantitative maps for proton spin density (PD) and T1 as well as volumes for gray matter, white matter and cerebrospinal fluid. All these contrasts are used to evaluate the presence of tumor, its

boundaries with surrounding tissues and how the tumor changes after radiation treatment. This study was carried out under collaboration with Henry Ford Medical Center, Cottage Hospital.

Chapter 2 includes the significance and value of quantitative maps and most powerful methods to develop quantitative mapping. Interest in quantitative mapping has emerged, and many methods have been developed to satisfy the interest. This chapter is dedicated to reviewing these methods.

Chapter 3 describes the methods and materials used in the thesis. This includes the STAGE concepts, supporting mathematical framework, initial protocol and phantom benchmarking. Since the original STAGE sequence was designed for 3T, the main effort of this study is translating STAGE to 0.35T. The main drawback of the 0.35T scanner is an inherently low signal to noise (SNR). By optimizing STAGE at 0.35T, the SNR issue was relatively improved.

Chapter 4 displays results of the phantom and patient data. An MRI system phantom has been developed through collaboration between the International Society of Magnetic Resonance in Medicine (ISMRM) ad-hoc committee on Standards for Quantitative Magnetic Resonance and the National Institute of Standards and Technology (NIST). The results are validated by the phantom and in agreement with the literature.

Chapter 5 presents the conclusion of the thesis and articulates future perspectives.

Chapter References

Delaney, G., Jacob, S., Featherstone, C., & Barton, M. (2005). The role of radiotherapy in cancer treatment: Estimating optimal utilization from a review of evidence-based clinical guidelines. *Cancer*, *104*(6), 1129–1137. https://doi.org/10.1002/cncr.21324

Han, S. J., Englot, D. J., Birk, H., Molinaro, A. M., Chang, S. M., Clarke, J. L., … Butowski, N. A. (2015). Impact of Timing of Concurrent Chemoradiation for Newly Diagnosed Glioblastoma: A Critical Review of Current Evidence. *Neurosurgery*, *62 Suppl 1*, 160–165. https://doi.org/10.1227/NEU.0000000000000801

Kontaxis, C. (2017). Towards real-time plan adaptation for MRI-guided radiotherapy. PhD Thesis, Utrecht University, The Netherlands

Mac Biedeman Mein IV, S. (2016). MRI-Guided Radation Therapy: Investigation the Accuracy of the Treatment Delivery, Master Thesis, Duke University, USA

Macklis, R. (2006). In regards to Hall: Intensity-modulated radiation therapy, protons, and the risk of second cancers (Int J Radiat Oncol Biol Phys 2006;65:1–7). *International Journal of Radiation Oncology*Biology*Physics*, *66*(5), 1593–1594. https://doi.org/10.1016/j.ijrobp.2006.06.058

Mittauer, K., Paliwal, B., Hill, P., Bayouth, J. E., Geurts, M. W., Baschnagel, A. M., … Bassetti, M. F. (2018). A New Era of Image Guidance with Magnetic Resonance-guided Radiation Therapy for Abdominal and Thoracic Malignancies. *Cureus*, *10*(4). https://doi.org/10.7759/cureus.2422

Mutic, S., & Dempsey, J. F. (2014). The ViewRay System: Magnetic Resonance-Guided and Controlled Radiotherapy. *Seminars in Radiation Oncology*, *24*(3), 196–199. https://doi.org/10.1016/j.semradonc.2014.02.008

Oelfke, U. (2015). Magnetic Resonance Imaging-guided Radiation Therapy: Technological Innovation Provides a New Vision of Radiation Oncology Practice. *Clinical Oncology*, *27*(9), 495–497. https://doi.org/10.1016/j.clon.2015.04.004

Shukla, G., Alexander, G. S., Bakas, S., Nikam, R., Talekar, K., Palmer, J. D., & Shi, W. (2017). Advanced magnetic resonance imaging in glioblastoma: a review. *Chinese Clinical Oncology*, *6*(4), 40. https://doi.org/10.21037/cco.2017.06.28

Siegel, R. L., Miller, K. D., & Jemal, A. (2019). Cancer statistics, 2019. *CA: A Cancer Journal for Clinicians*, *69*(1), 7–34. https://doi.org/10.3322/caac.21551

Society, N. B. T. (2019). *Quick Brain Tumor Facts*. *2019*.

Sulman, E. P., Ismaila, N., Armstrong, T. S., Tsien, C., Batchelor, T. T., Cloughesy, T., … Chang, S. M. (2017). Radiation Therapy for Glioblastoma: American Society of Clinical Oncology Clinical Practice Guideline Endorsement of the American Society for Radiation Oncology Guideline. *Journal of Clinical Oncology : Official Journal of the American Society of Clinical Oncology*, *35*(3), 361–369. https://doi.org/10.1200/JCO.2016.70.7562

Tsien, C., Gomez-Hassan, D., Ten Haken, R. K., Tatro, D., Junck, L., Chenevert, T. L., & Lawrence, T. (2005). Evaluating changes in tumor volume using magnetic resonance imaging during the course of radiotherapy treatment of high-grade gliomas: Implications for conformal dose-escalation studies. *International Journal of Radiation Oncology, Biology, Physics*, *62*(2), 328–332. https://doi.org/10.1016/j.ijrobp.2004.10.010

Yang, Z., Zhang, Z., Wang, X., Hu, Y., Lyu, Z., Huo, L., … Hong, J. (2016). Intensity-modulated radiotherapy for gliomas:dosimetric effects of changes in gross tumor volume on organs at risk and healthy brain tissue. *OncoTargets and Therapy*, *9*, 3545–3554. https://doi.org/10.2147/OTT.S100455

Zschaeck, S., Wust, P., Graf, R., Misch, M., Onken, J., Ghadjar, P., … Kaul, D. (2018). Locally dose-escalated radiotherapy may improve intracranial local control and overall survival among patients with glioblastoma. *Radiation Oncology*, *13*(1), 251. https://doi.org/10.1186/s13014-018-1194-8

Chapter 2

Literature Review

2.1 Quantitative Magnetic Resonance Imaging (qMRI)

Quantitative imaging is inherently accompanied by greater visualization, sensitivity and precision in comparison to qualitative imaging (Ma, 2015). This can be explained with the following reasons:

Quantitative magnetic resonance imaging (qMRI) maps reveal the natural characteristics of human body tissues. While some details and fine structures cannot be observed by weighted imaging, they may be detectable in corresponding quantitative images. Weighted images are developed based on the integration of many parameters. Despite their potential to highlight a specific parameter, the contrast between adjacent tissues may be eliminated due to the integration of other parameters (Ma, 2015).

Quantitative values associate with physiological properties directly. As a result, qMRI enables the potential for the early detection of pathological changes the assessment of treatment response with more sensitivity (Ma, 2015).

qMRI enables longitudinal comparison with multi-center data. The signal of the qualitative images may not be time independent as it may change from time to time because of possible changes in the acquisition setting. In other words, qMRI demonstrated more precision and reproducibility (Ma, 2015).

2.1.1 Clinical Significance of qMRI (NMR relaxation times)

There has been substantial interest in quantifying T1 (spin-lattice) and T2 (spin-spin) proton (^{1}H) nuclear magnetic resonance (NMR) relaxation times. Damadian et al. reported higher T1 and T2 in cancerous cells compared with normal cells in a rat experiment. In their experiment malignant tumor relaxation times were twofold higher than with normal tissues and a benign studied tumor, prompting the idea that relaxation times might have diagnostic value in detecting malignant tumors (Damadian, Zaner, Hor, & DiMaio, 1971). The study was replicated by Weisman et al in tumorous rat tail in vivo (Weisman, Bennett, Maxwell, Woods, & Burk, 1972).

Frey et al observed that the T1 value was 15% up to 20% greater in some tumor-bearing animals compared with animals without tumors, suggesting systematic effects

(Frey et al., 1972). Hazlewood et al extended Damadian et al's experiment to preneoplastic tissues and breast tumor (Hazelwood, Chang, Medina, Cleveland, & Nichols, 1972). Also, they conducted an experiment on immature muscle and perceived higher relaxation times, which implied that elevation in relaxation times was not specific to tumors (Hazlewood, Nichols, Chang, & Brown, 1971).

An early experiment on human tumors was conducted by Cottam et al. In the study, three out of five different tumors indicated T1 values overlapped with the T1 values from various normal tissue (Cottam, Vasek, & Lusted, 1972). Later, Hollis et al found higher T1 values in tumors in three out of four patients. In the fourth patient, a lung adenocarcinoma could not be discriminated from control lung tissue with atelectasis, inflammation and calcified granuloma (Hollis et al., 1973). This suggests that noncancerous abnormal tissue might also generate greater T1 values.

However, Damadian et al revealed the opposite results (Damadian, Zaner, Hor, & Dimaio, 1973), (Damadian, Zaner, Hor, DiMaio, et al., 1973). They investigated 106 human tumors located in various organs and stated that T1 values were significantly higher than the corresponding T1 values of normal tissue from the same organ. There was an exception for melanoma, which indicated a lower T1 value. This finding differed from Hollis et al's mouse experiment. Damadian et al justified their finding by showing the paramagnetic characteristic properties of melanin. Another researcher described some overlapping malignant tumors' T1 value with the T1 of normal tissue from different organs, but the probability that the mean of the T1s of various organs' cancer cells did not deviate significantly from normal tissue from the same organs was less than 0.01 (Fung, 1977).

The change in NMR relaxation times has been attributed to the change of water content, the interaction of water molecule with the microstructure of the body and iron accumulation (Kiricuta & Simplaceanu, 1975), (Vymazal et al., 1995). It was shown that in neurodegenerative disease, excess iron was observed (Hagemeier, Geurts, & Zivadinov, 2012). Patients who suffer from Parkinson's disease and multiple system atrophy demonstrated shortened T1 and T2 in the putamen and globus pallidus because of iron accumulation (Vymazal et al., 1999).

2.1.2 qMRI for characterizing tumor response

Quantitative MRI (qMRI) has demonstrated remarkable promise for characterizing tumor margins, investigating invasion (Price & Gillard, 2011) and quantifying tumor changes after treatment (Deng & Wang, 2017). However, limited qMRI has been performed using MRgRT for data acquired during RT treatment. The first study of tumor response assessment was based on variations changes in the apparent diffusion coefficient (ADC) maps derived from diffusion weighted imaging for a 0.35T MR-Co 60 RT system (Deng & Wang, 2017). The study clearly highlighted the plausibility of the system for tracking tumor response. The study did not include any adaptation of the RT treatment course, and only diffusion-based biomarkers were utilized.

It has been proven that R2* map values can be used as a discernable indication of tumor malignancy and identification of the grade of gliomas and R2* value can define gliomas better than ADC values (Liu, Liao, Yin, & Li, 2014).

Quantitative T1 map values are able to depict early tumor response (McSheehy et al., 2010) and recognizing enhanced tumors earlier than conventional contrast-enhanced T1-weighted images (Lescher et al., 2015)

2.2 Quantitative Mapping Approaches

Because of the diagnostic potential of T1 and T2 in detecting pathology, many methods have been developed to quantify T1 and T2 maps. The methods can be characterized into two categories (Ma, 2015):

1. Single Parametric Methods
2. Multi Parametric Methods

In the following, both approaches will be delineated.

2.2.1 Single Parametric Methods

The aim of these methods is quantifying a single parameter during each acquisition time. It was assumed that the effects of other parameters in acquisition time are negligible. The most pivotal approach to measuring T1 is based on utilizing spin echo (SE) as a function of relative proton density, T1 and T2 (Brown, Cheng, & Haacke, 2014):

$$S(t) = M_0\left(1 - e^{-\frac{TR}{T1}}\right)e^{-\frac{TE}{T2}} \tag{2.1}$$

Where S is the signal, M_0 is the proton density, TR is repetition time and TE is echo time.

Three scans are required to extract M_0, T1 and T2. The first one finds M_0 by choosing TE and TR as $TR \gg T1,\ \ TE \ll T2$

$$M_0 = S(TR \gg T1,\ \ TE \ll T2) \tag{2.2}$$

Once M_0 is determined, T1 is measurable in the second scan when TR is relatively shorter than T1

$$S(TR \ll T1,\ \ TE \ll T2) \approx\ M_0 * \frac{TR}{T1} \tag{2.3}$$

$$\Rightarrow T1 = \frac{M_0 T_R}{M_{xy}(TR \ll T1,\ \ TE \ll T2)} = T_R * \frac{S(TR \gg T1,\ \ TE \ll T2)}{S(TR \ll T1,\ \ TE \ll T2)} \tag{2.4}$$

In practice, the second scan has low SNR, and averaging over multiple acquisition is needed for a reasonable SNR. This problem, plus long TR to get M_0, makes this method clinically useless.

This method was further improved by adding an inversion recovery (IR) pulse at the beginning of each acquisition and acquiring a series of images by increasing the inversion time (TI) (Crawley & Henkelman, 1988):

$$S(t) = M_0\left(1 - 2e^{-\frac{TI}{T1}} - e^{-\frac{TR}{T1}}\right)e^{-\frac{TE}{T2}} \tag{2.5}$$

SE and IR are based on employing multi points in the relaxation exponential curve. The multi-point measurement method is susceptible to systematic error due to imperfections in the FA that can be minimized by acquiring a large number of points (N). The SE method utilizes N points in an exponential decay curve with varying TRs, while IR does it with increasing TIs. Since they are a 2D sequence, the acquisition time is long. In clinical applications, increasing the phase encodes lines with a long TR (conventionally larger than highest T1 value in the region of interest imaging), which makes this approach infeasible. For example, 256*128 pixels image, with N=5 and TR=5 s, requires 128*5*5 s. i.e., 54 min for a single slice.

To alleviate this issue, the use of simulated echoes (ST) has been developed as a potential solution for the “one shot” approach to T1 quantification. One-shot refers to collecting all the points along the relaxation curve in a single excitation. Look and Locker (LL) proposed a new one-shot method in which its basic principle is based on following an inversion recovery pulse; the recovery of the longitudinal magnetization of the steady state is progressively sampled by a train of small FA, and during the T1 relaxation curve, all points are measured (Look & Locker, 1970). The transition state of the relaxation can be modeled by the IR formula but with a modulation of the relaxation time T1(T_1^*):

$$T1^* = \frac{T1}{1 - \frac{T1}{\tau}\ln(\cos\theta)} \qquad (2.6)$$

Where τ is the time between each consecutive element of the train of FA (θ).

The acquisition time for one-shot driven methods is more reasonable than the multi points method (IR and SE). The use of a restricted number of FAs in one-shot driven methods inherently prompts a reduction in SNR. However, the reduced imaging time allows for more signal averaging over a long acquisition time, which will relativelyimprove SNR. Figure 5 depicts a schematic overview of the signal behavior for LL method.

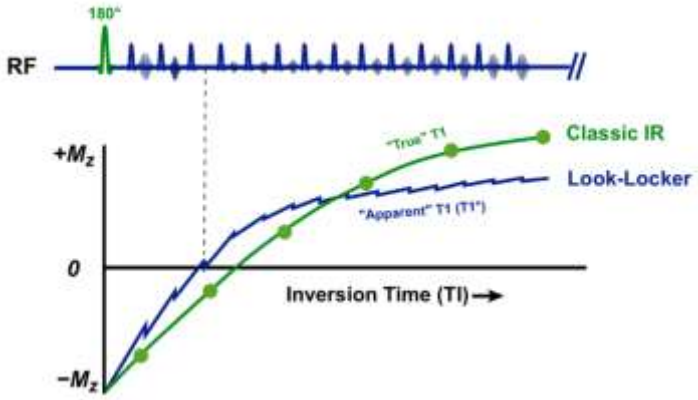

Figure 4. A schematic plot of the LL sequence. The IR sequence is very inefficient because of the long recovery period. To overcome this problem, longitudinal magnetization should be sampled by applying a train of small FA (θ) RF pulses during the repletion time. A separate phase encoding the gradient of the same value is applied for each θ pulse and there is no residual transverse magnetization before each new pulse. If the separation time is τ, the required time for sampling n pints is $n * \tau$. Indeed, it is efficient to consider TR= $n * \tau$. In fact, the n images reconstructed represent samples of the inversion recovery curve at inversion times TI = {0, τ, $2 * \tau$,…,$n * \tau$ }; however, due to applying consecutive RF pulse, the apparent TI is slightly different. [3]

2.2.1.1 Efficiency

Consider the MR scanner in the 'spectrometer' (all gradients are off) and the acquired signal of a multipoint T1 sequence without averaging along the relaxation curve at time t as $S(t)$ and the standard deviation of σ_0 for the additive white noise. DR (for here) for the multipoint experiment is defined as $DR = S(0) - S(\infty)$. The SNR of the data before any signal averaging is given by $\frac{DR}{\sigma_0}$ (Crawley & Henkelman, 1988). An estimation of T1 can be determined from these data by applying a least square fitting procedure. The noise propagation of the least square can be categorized by (Crawley & Henkelman, 1988):

$$b = \frac{\frac{\sigma_{T1}}{T1}}{\frac{\sigma_0}{DR}} \qquad (2.7)$$

The noise factor b depends on the sampling time at the T1 relaxation curve (for the LL method on the limited FA). In the MR conventional mode, the 2D Fourier transform imaging process performs N_{pe} signal averaging on each pixel signal, where N_{pe} is the

[3] The image is adapted from http://mriquestions.com/t1-mapping.html

number of phase encode lines. If the sequence is repeated N_{ex} times for each phase encode line, we have $N_{rep} = N_{ex}N_{rep}$. The scan time T_{exam} is equal to $T_{exam} = N_{rep} * T_{seq}$. The SNR is given by (Crawley & Henkelman, 1988):

$$\frac{T1}{\sigma_{T1}} = \frac{DR}{\sigma_0} * \frac{1}{b}\sqrt{N} = \frac{DR}{\sigma_0} * \frac{1}{b}\sqrt{\frac{T_{exam}}{T_{seq}}} \qquad (2.8)$$

It is reasonable to compare the efficiency of multipoint T1 sequences in terms of the SNR of the calculated T1 image made in a constant exam time. Thus, by setting T_{exam} and σ_0 as a unity, the efficiency is given by:

$$\Gamma = \frac{DR}{b\sqrt{T_{seq}}} \qquad (2.9)$$

The efficiency Γ increment is characterized by increasing the DR, minimizing the scan time and optimizing the sampling times. The dynamic range of the IR is double that of the SE, which explains the reason for the popularity of this sequence. The LL method has a slightly smaller DR; however, its scanning time is much shorter, and the possibility of averaging improves the signal.

It has been affirmed that the IR method has higher efficiency compared to SE due to its larger dynamic range. The imaging method with a fast readout can mitigate long acquisition time such as echo planer imaging (EPI) (Clare & Jezzard, 2001) or fast low angle shot (FLASH) (Haase, Frahm, Matthaei, Hanicke, & Merboldt, 2011). The LL method has efficiency at the same level as the IR method with shorter imaging time. e.g. whole brain volume with 1.4*1.4*5 mm^3 can be imaged by LL in 8 minutes (Crawley & Henkelman, 1988).

2.2.1.2 Steady State Sequences

Steady state sequences have significantly shorter acquisition time than other sequences, which enables them to be proper candidates for clinical T1 mapping. The signal of the spoiled gradient echo (or gradient recall echo (GRE) or FLASH) at the echo time, assuming $TE \ll T2^*$, is equal to:

$$S(\theta) = M_0 \frac{(1 - E_1)\sin\theta}{1 - E_1 \cos\theta} \tag{2.10}$$

Where $E_1 = e^{-\frac{TR}{T1}}$, θ is flip angle (FA).

If TR is kept constant and θ is increased gradually, T1 and M_0 can be determined by a linear equation:

$$\frac{S(\theta)}{\sin\theta} = E_1 \frac{S(\theta)}{\tan\theta} + M_0(1 - E_1) \tag{2.11}$$

The slope m and intercept b can be estimated by a simple regression, which gives T1 and M_0(PD) simultaneously:

$$T_1 = \frac{-TR}{\ln(m)} \qquad M_0 = \frac{b}{1 - m} \tag{2.12}$$

Early attempts to initiate this method were done by Fram et al, who acquired 5 images with variable FA to quantify a 2D T1 map in 3.4 minutes (Fram et al., 1987). More improvement for fast and efficient imaging was suggested by Deoni et al by defining a mathematical framework to find two optimum FAs to image whole brain volume (DESPOT1) (Deoni, Rutt, & Peters, 2003). By defining two terms named ‘dynamic range (DR)’ and ‘fractional signal (FS)’, they showed that precision can be maximized if the product of DR and FS is maximized.

$$DR = \frac{S(\theta_2)}{M_0 \sin(\theta_2)} - \frac{S(\theta_1)}{M_0 \sin(\theta_1)} \tag{2.13}$$

$$FS = \frac{S(\theta_1) + S(\theta_2)}{2S(\theta_E)} \tag{2.14}$$

Where θ_1, θ_2 and θ_E are the pair of optimum FAs, the Ernst angle, respectively, and $S(\theta_1)$, $S(\theta_2)$ and $S(\theta_E)$ are the signal associated with θ_1, θ_2 and θ_E, respectively. Figure 6 the 2D contour plot of the product of DR and FS for the choice of two optimum FAs.

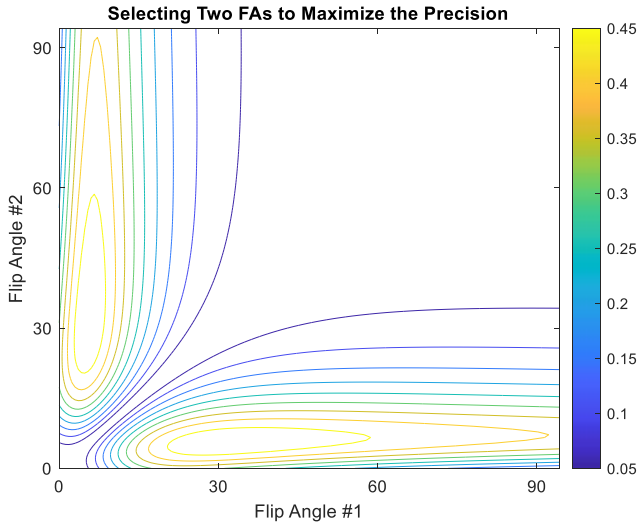

Figure 5. A 2D contour plot to choose a pair of optimum FAs based on Deoni et al's method. The plot is symmetrical, which suggests that FAs can be selected from each axis.

Deoni showed that two optimum FAs are enough for T1 brain mapping. By using DESPOT1, the whole brain volume with 1*1*1 mm^3 resolution was imaged in 8 minutes. DESPOT1 has 3.3 times more efficiency than the multi-point (N=8) IR method.

Deoni et al. upgraded the DESPOT1 approach to DESPOT2 (Deoni et al., 2003) as a quick T2 map measurement. The idea is based on integration of steady state free precision (SSFP) and spoiled gradient echo. By assuming that off-resonance equals π every, the SSFP equation is simplified to:

$$S = \frac{M_0(1 - E_1) * \sin\theta}{1 - E_1E_2 - (E_1 - E_2)\cos\theta} \tag{2.15}$$

Where $E_{1,2} = e^{-\frac{TR}{T_{1,2}}}$

As with DESPOT1, by keeping TR at a constant value and continuously increasing FA, T2 is determined by a linear equation, which is a simple regression that can render its slope (m) and intercept (b):

$$\frac{S_{ssfp}}{\sin(\alpha)} = \frac{E_1 - E_2}{1 - E_1E_2} * \frac{S_{ssfp}}{\tan(\alpha)} + \frac{M_0(1 - E_1)}{1 - E_1E_2} \tag{2.16}$$

Once T1 (and hence E1) is known, T2 and M_0 (PD) can be estimated by m and b:

$$T_2 = -\frac{TR}{\ln\left(\frac{m - E_1}{mE_1 - 1}\right)} \qquad M_0 = \frac{b(E_1E_2 - 1)}{1 - E_1} \tag{2.17}$$

The total time for the whole coverage of brain T2 mapping with isotropic 1mm^3 resolution is about 8 minutes, which is 2.65 times more efficient than spin echo (SE), the gold standard for T2 mapping. Although DESPOT2 is more efficient than SE, it is sensitive to B_0 inhomogeneities. In the absence of perfect shimming, DESPOT2 can be severely damaged. It should be noted that SE is based on the full relaxation of longitudinal magnetization since T2 is measured with incremented TEs with $TR \gg T1$ assumption, which is time consuming. Multi refocused spin echo was introduced to ease the long imaging problem (Feinberg et al., 1985). It was suggested that during TR $\sim$5 s, readouts from separate planar volumes in the subject were measured without affecting adjacent imaged areas.

2.2.2 Multi-Parametric methods

Multi-parametric methods quantify multiple quantitative maps in one single acquisition. These methods can be characterized into two categories (Ma, 2015):

The first type was established to have two different types of sensitivity encoding in one sequence. Quantification of relaxation times and proton density by twin-echo saturation recovery turbo field echo (QRAPTEST) (Warntjes, Dahlqvist, & Lundberg, 2007) and quantification of relaxation times and proton density by multi-echo acquisition of a saturation recovery using turbo spin echo (QRAPMASTER) (Warntjes, Dahlqvist Leinhard, West, & Lundberg, 2008) are two well-known methods which quantify T1 by SR- Look Locker and IR, respectively. They quantify T2 by a multi echo sequence with a fast readout. PD can be estimated by a scaling factor of fitting between the acquired signal and the theory model. Their acquisition time is in a clinically acceptable range (5 minutes) to quantify T1, T2 and PD from 20 slices with 0.8*0.8 mm^2 resolution for QRAMASTER.

The second type was established to fit an acquired signal, which is a mixture of multiple parameters of an assumed model to extract parameters. This enables researchers to find maps fitting the signal to the signal model. There has been interest in the IR TrueFISP (bSSFP) sequence for quantification of T1, T2 and PD from a single IR TrueFISP signal time course (Schmitt et al., 2004). A mono-exponential behavior approximation to estimate temporal behavior of TrueFISP sequence, by assuming off-resonance at zero and prepared with initial RF pulse $\frac{\theta}{2}$, was proposed:

$$E_1^* = E_1 \cos^2\frac{\theta}{2} + E_2 \sin^2\frac{\theta}{2} \tag{2.18}$$

Where θ represents the flip angle and $E_{1,2} = e^{-\frac{TR}{T_{1,2}}}$. This equation (2.18) can be simplified to the following equation if $TR \ll T1{,}2$

$$T1^* = \left(\frac{1}{T1}\cos^2\frac{\theta}{2} + \frac{1}{T2}\sin^2\frac{\theta}{2}\right)^{-1} \tag{2.19}$$

$T1^*$denotes apparent relaxation times.

Assuming that $t = 0$ is positioned at the first imaging pulse, the TrueFISP signal at the beginning can be extrapolated to

$$S_0 = M_0 \sin\frac{\theta}{2} \tag{2.20}$$

TrueFISP at steady state signal may be noted as

$$S_{stst} = \frac{M_0(1-E_1)\sin\theta}{1-(E_1-E_2)\cos\theta - E_1E_2} \approx \frac{M_0\sin\theta}{\left(\frac{T_1}{T_2}+1\right) - \cos\theta\left(\frac{T_1}{T_2}-1\right)} \tag{2.21}$$

In general, S_{stst} is lower than the initial signal S_0. Hence, three parameters are required to model IR temporal signal behavior from S_0 to S_{stst}. e.g., using the fit function

$$S(nTR) = S_{stst}\left[1 - INV * e^{\left(-\frac{nTR}{T_1^*}\right)}\right] \tag{2.22}$$

INV denotes inversion factor indicating the ratio between S_0 and S_{stst}. By integrating equation (2.20) and (2.21), INV can be found as

$$INV = 1 + \frac{S_0}{S_{stst}} = 1 + \frac{\sin\frac{\theta}{2}}{\sin\theta}\left[\left(\frac{T_1}{T_2} + 1\right) - \cos\theta\left(\frac{T_1}{T_2} - 1\right)\right] \quad (2.23)$$

This shows that INV only depends on the FA and $\frac{T_1}{T_2}$, approximating INV=2 for the small flip angle. With equation (2.19), the parameters can be expressed as:

$$T_1 = T_1^* \cos\frac{\theta}{2}(INV - 1) \quad (2.24)$$

$$T_2 = T_1^* sin^2\frac{\theta}{2}\left(1 - \frac{\cos\frac{\theta}{2}}{INV - 1}\right)^{-1} \quad (2.25)$$

$$M_0 = \frac{S_{stst}(INV - 1)}{\sin\frac{\theta}{2}} \quad (2.26)$$

All approaches can be accelerated by combining the benefits of the spatial and temporal redundancy of the signal. The special-redundancy-based methods are mainly founded by exploiting the correlations in k-space, comprises partial Fourier method, reduced field of view methods and parallel imaging (Ma, 2015). These methods expedite scanning time by acquiring a portion of the k-space. The temporal-redundancy-based methods assume that the dynamic range of successive time point is small and the signal can be simplified to a mathematical model (Ma, 2015).

Chapter References

Brown, R., Cheng, Y., & Haacke, E. (2014). *Magnetic Resonance Imaging: Physical Properties and Sequence Design* (2nd Editio). Retrieved from https://onlinelibrary.wiley.com/doi/book/10.1002/9781118633953

Clare, S., & Jezzard, P. (2001). Rapid T1 mapping using multislice echo planar imaging. *Magnetic Resonance in Medicine*, *45*(4), 630–634. https://doi.org/10.1002/mrm.1085

Cottam, G. L., Vasek, A., & Lusted, D. (1972). Water proton relaxation rates in various tissues. *Research Communications in Chemical Pathology and Pharmacology*, *4*(3), 495–502.

Crawley, A. P., & Henkelman, R. M. (1988). A comparison of one-shot and recovery methods in T1 imaging. *Magnetic Resonance in Medicine*, *7*(1), 23–34.

Damadian, R., Zaner, K., Hor, D., & Dimaio, T. (1973). Human tumors by NMR. *Physiological Chemistry and Physics*, *5*(5), 381–402.

Damadian, R., Zaner, K., Hor, D., & DiMaio, T. (1974). Human tumors detected by nuclear magnetic resonance. *Proceedings of the National Academy of Sciences of the United States of America*, *71*(4), 1471–1473. https://doi.org/10.1073/pnas.71.4.1471

Damadian, R., Zaner, K., Hor, D., DiMaio, T., Minkoff, L., & Goldsmith, M. (1973). Nuclear magnetic resonance as a new tool in cancer research: human tumors by NMR. *Annals of the New York Academy of Sciences*, *222*, 1048–1076.

Deng, J., & Wang, Y. (2017). Quantitative magnetic resonance imaging biomarkers in oncological clinical trials: Current techniques and standardization challenges. *Chronic Diseases and Translational Medicine*, *3*(1), 8–20. https://doi.org/10.1016/j.cdtm.2017.02.002

Deoni, S. C. L., Rutt, B. K., & Peters, T. M. (2003). Rapid combined T1 and T2 mapping using gradient recalled acquisition in the steady state. *Magnetic Resonance in Medicine*, *49*(3), 515–526. https://doi.org/10.1002/mrm.10407

Feinberg, D. A., Mills, C. M., Posin, J. P., Ortendahl, D. A., Hylton, N. M., Crooks, L.

E., … Hoenninger, J. C. (1985). Multiple spin-echo magnetic resonance imaging. *Radiology*, *155*(2), 437–442. https://doi.org/10.1148/radiology.155.2.3983396

Fram, E. K., Herfkens, R. J., Johnson, G. A., Glover, G. H., Karis, J. P., Shimakawa, A., … Pelc, N. J. (1987). Rapid calculation of T1 using variable flip angle gradient refocused imaging. *Magnetic Resonance Imaging*, *5*(3), 201–208. https://doi.org/https://doi.org/10.1016/0730-725X(87)90021-X

Frey, H. E., Knispel, R. R., Kruuv, J., Sharp, A. R., Thompson, R. T., & Pintar, M. M. (1972). Proton spin-lattice relaxation studies of nonmalignant tissues of tumorous mice. *Journal of the National Cancer Institute*, *49*(3), 903–906.

Fung, B. M. (1977). Correlation of relaxation time with water content in muscle and brain tissues. *Biochimica et Biophysica Acta*, *497*(1), 317–322.

Haase, A., Frahm, J., Matthaei, D., Hanicke, W., & Merboldt, K.-D. (2011). FLASH imaging: rapid NMR imaging using low flip-angle pulses. 1986. *Journal of Magnetic Resonance (San Diego, Calif. : 1997)*, *213*(2), 533–541. https://doi.org/10.1016/j.jmr.2011.09.021

Hagemeier, J., Geurts, J. J. G., & Zivadinov, R. (2012). Brain iron accumulation in aging and neurodegenerative disorders. *Expert Review of Neurotherapeutics*, *12*(12), 1467–1480. https://doi.org/10.1586/ern.12.128

Hazelwood, C. F., Chang, D. C., Medina, D., Cleveland, G., & Nichols, B. L. (1972). Distinction between the preneoplastic and neoplastic state of murine mammary glands. *Proceedings of the National Academy of Sciences of the United States of America*, *69*(6), 1478–1480. https://doi.org/10.1073/pnas.69.6.1478

Hazlewood, C. F., Nichols, B. L., Chang, D. C., & Brown, B. (1971). On the state of water in developing muscle: a study of the major phase of ordered water in skeletal muscle and its relationship to sodium concentration. *The Johns Hopkins Medical Journal*, *128*(3), 117–131.

Hollis, D. P., Economou, J. S., Parks, L. C., Eggleston, J. C., Saryan, L. A., & Czeister, J. L. (1973). Nuclear magnetic resonance studies of several experimental and human malignant tumors. *Cancer Research*, *33*(9), 2156–

2160.

Kiricuta, I. C. J., & Simplaceanu, V. (1975). Tissue water content and nuclear magnetic resonance in normal and tumor tissues. *Cancer Research*, *35*(5), 1164–1167.

Lescher, S., Jurcoane, A., Veit, A., Bahr, O., Deichmann, R., & Hattingen, E. (2015). Quantitative T1 and T2 mapping in recurrent glioblastomas under bevacizumab: earlier detection of tumor progression compared to conventional MRI. *Neuroradiology*, *57*(1), 11–20. https://doi.org/10.1007/s00234-014-1445-9

Liu, Z., Liao, H., Yin, J., & Li, Y. (2014). Using R2* values to evaluate brain tumours on magnetic resonance imaging: preliminary results. *European Radiology*, *24*(3), 693–702. https://doi.org/10.1007/s00330-013-3057-x

Look, D. C., & Locker, D. R. (1970). Time Saving in Measurement of NMR and EPR Relaxation Times. *Review of Scientific Instruments*, *41*(2), 250–251. https://doi.org/10.1063/1.1684482

Ma, D. (2015). Magnetic Resonance Fingerprinting. PhD Thesis, Case Western Reverse University, USA

McSheehy, P. M. J., Weidensteiner, C., Cannet, C., Ferretti, S., Laurent, D., Ruetz, S., … Allegrini, P. R. (2010). Quantified tumor t1 is a generic early-response imaging biomarker for chemotherapy reflecting cell viability. *Clinical Cancer Research : An Official Journal of the American Association for Cancer Research*, *16*(1), 212–225. https://doi.org/10.1158/1078-0432.CCR-09-0686

Price, S. J., & Gillard, J. H. (2011). Imaging biomarkers of brain tumour margin and tumour invasion. *The British Journal of Radiology*, *84 Spec No 2*, S159-67. https://doi.org/10.1259/bjr/26838774

Schmitt, P., Griswold, M. A., Jakob, P. M., Kotas, M., Gulani, V., Flentje, M., & Haase, A. (2004). Inversion Recovery TrueFISP: Quantification of T1, T 2, and Spin Density. *Magnetic Resonance in Medicine*, *51*(4), 661–667. https://doi.org/10.1002/mrm.20058

Vymazal, J., Brooks, R. A., Patronas, N., Hajek, M., Bulte, J. W., & Di Chiro, G. (1995). Magnetic resonance imaging of brain iron in health and disease. *Journal*

of the Neurological Sciences, *134 Suppl*, 19–26.

Vymazal, J., Righini, A., Brooks, R. A., Canesi, M., Mariani, C., Leonardi, M., & Pezzoli, G. (1999). T1 and T2 in the brain of healthy subjects, patients with Parkinson disease, and patients with multiple system atrophy: relation to iron content. *Radiology*, *211*(2), 489–495. https://doi.org/10.1148/radiology.211.2.r99ma53489

Warntjes, J. B. M., Dahlqvist Leinhard, O., West, J., & Lundberg, P. (2008). Rapid magnetic resonance quantification on the brain: Optimization for clinical usage. *Magnetic Resonance in Medicine*, *60*(2), 320–329. https://doi.org/10.1002/mrm.21635

Warntjes, J. B. M., Dahlqvist, O., & Lundberg, P. (2007). Novel method for rapid, simultaneous T1, T2*, and proton density quantification. *Magnetic Resonance in Medicine*, *57*(3), 528–537. https://doi.org/10.1002/mrm.21165

Weisman, I. D., Bennett, L. H., Maxwell, L. R., Woods, M. W., & Burk, D. (1972). Recognition of Cancer in vivo by Nuclear Magnetic Resonance. *Science*, *178*(4067), 1288 LP – 1290. https://doi.org/10.1126/science.178.4067.1288

Chapter 3

STrategically Acquired Gradient Echo (STAGE):

Concept and Translation to

0.35T MR-linac

Introduction

The initial idea of using a variable flip angle was established by Gupta et al (Gupta, 1977) and Venkatesan (Venkatesan, Lin, & Haacke, 1998). The method was based on the acquisition of a few spoiled gradient echoes (or a gradient recall echo (GRE)) which were differentiated with various FAs to quantify T1 and PD simultaneously. The variable flip angle (VFA) has attracted interest over time; however, its applications were limited to quantifying T1 and PD.

Strategically acquired gradient echo (STAGE) was introduced as a potential brain imaging protocol offering multiple types of quantitative tissue property information and qualitative brain imaging in a clinically acceptable range (<10 minutes) at 3T (Chen, Liu, Wang, Kang, & Haacke, 2018) , (Wang et al., 2018). STAGE employs a set of spoiled gradient echo acquisitions with optimal echo times, flip angles and flow re-phasing/dephasing strategies to obtain multi-contrast qualitative images and quantitative data for studying various neurodegenerative diseases. It takes 5 min at 3T for T1 weighted enhanced, T1 weighted, PD weighted, T1 map, PD map, SWI, tSWI, QSM and R2* map covering the whole brain. With another 5 min, one can also get the MRAV, MRA as well as co-registered QSM, tSWI and R2*map from the same scan for entire cerebral vascular visualization and quantification, especially for small arteries and veins.

In this chapter STAGE concepts will be reviewed and the procedure for translating STAGE from 3T to 0.35T will be discussed. The results will be validated by a phantom experiment and patients' data.

3.1 Strategically acquired gradient echo (STAGE)

3.1.1 STAGE concept

STAGE consists of two triple-echo GRE scans acquired by two optimal flip angles. The first one is smaller than the Ernst angle and is proton density weighted (PDW). The second one is larger than the Ernst angle and T1 weighted (T1W). It has been shown that two optimum flip angles are enough to quantify T1 and PD maps for whole brain volume. Despite STAGE's capabilities to quantify B1 field variation, no RF transmit field effect and B1 correction has been applied for T1 mapping because of the low field used. To maximize the contrast between gray matter (GM) and white

matter (WM), T1 weighted enhanced (T1WE) image is proposed. The final T1WE image is based on the average of each echo. All echo times are fully compensated by nulling zero and the first gradient moment. In this study, we did not use the STAGE potential to produce QSM and SWI maps because of the limitations of echo time and magnetic field strength. An R2* map was generated from each flip angle separately and then averaged. Simulated Flair was produced by combining the PD map and T1 map and a reasonable estimation of the T2 map.

3.1.2 Theory and simulation

The signal intensity of the spoiled gradient echo as a function of FA (θ) can be expressed by the Ernst equation:

$$S(\theta) = M_0 \sin\theta \frac{1 - E_1}{1 - \cos\theta * E_1} * e^{-\frac{TE}{T2^*}} \tag{3.1}$$

While FAs smaller than the Ernst angle tend to make the image PDW, larger ones tend to make the image T1W. For a given FA, the contrast between GM and WM is confined to the T1 ratio of GM over WM. To quantify the contrast, it is beneficial to investigate the contrast to noise ratio (CNR) defined as:

$$CNR_{gre} = \frac{|S_{WM}(\theta) - S_{GM}(\theta)|}{\sigma_0} \tag{3.2}$$

Where $S_{WM/GM}$ denotes the signal mean value for WM and GM on the default region, and σ_0 is the image noise standard deviation. However, there is a novel way to increase the contrast between WM and GM: by subtracting the two signals (images). In this case, in the CNR formula, σ_0 should be replaced with $\sqrt{2}\sigma_0$. Hence, the GM/WM CNR of the subtraction of two variant signals with corresponding θ_1 and θ_2, can be described as:

$$CNR_{sub} = \frac{|(S_{WM}(\theta_2) - S_{WM}(\theta_1)) - (S_{GM}(\theta_2) - S_{GM}(\theta_1))|}{\sqrt{2}\sigma_0} \tag{3.3}$$

To verity that subtraction amplifies the CNR, a simulation was performed based on equations (3.1) - (3.3) with the following parameters (Bottomley, Foster, Argersinger, & Pfeifer, 1984):

$$TR = 40ms, \quad TE = 5ms, \quad M_{0_{GM}} = 0.85, \quad T1_{GM} = 575, \quad T2*_{GM} = 60ms,$$
$$M_{0_{WM}} = 0.7, \quad T1_{WM} = 472, \quad T2*_{WM} = 40ms$$

In the simulations, σ_0 is considered equal to one. Figure 7 illustrates S_{GM}, S_{WM}, CNR_{gre} and CNR_{sub} as a function of FA. To maximize efficiency, θ_1 is considered as a given value and θ_2 was discovered such that CNR_{sub} meets the maximum value. Simulations proved that CNR_{sub} is greater than CNR_{gre}.

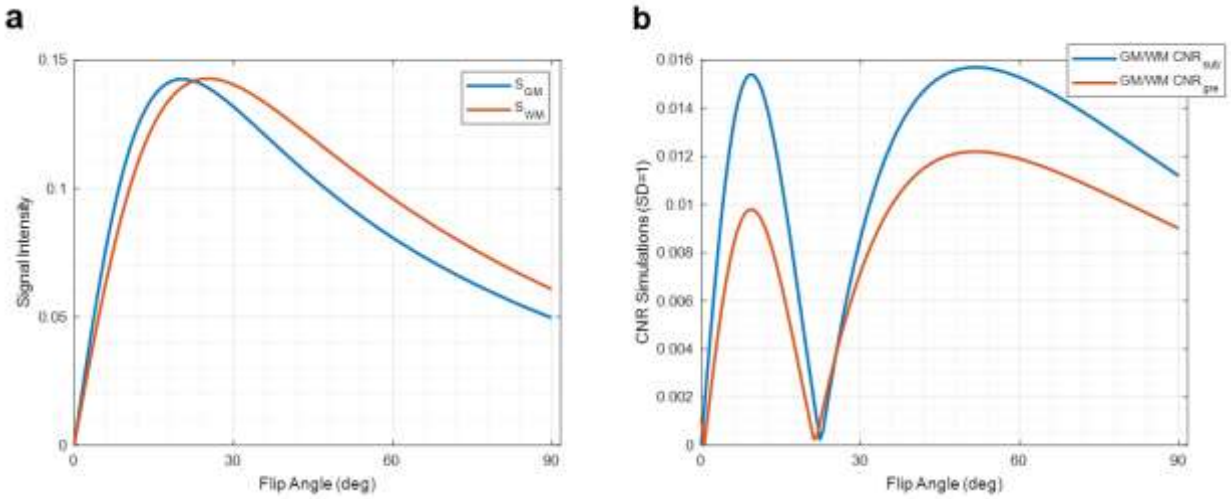

Figure 6. a) Spoiled gradient signal as a function of FA for WM and GM based on equation (3.1), b) CNR_{gre} and CNR_{sub} based on equations (3.2) and (3.3) with described parameters, respectively. The maximum CNR_{sub} achieved at $\alpha_1 = 10°$ and $\alpha_2 = 58°$.

As mentioned in the previous chapter, Deoni et al (Deoni, Rutt, & Peters, 2003) defined the precision of the whole brain T1 mapping derived from two FAs by maximizing the product of the dynamic range (DR) of the regression line and the fractional signal (FS) of the points, given by

$$DR * FS = \left[\frac{S(\theta_2)}{M_0 \sin(\theta_2)} - \frac{S(\theta_1)}{M_0 \sin(\theta_1)}\right] * \left[\frac{S(\theta_1) + S(\theta_2)}{2S(\theta_E)}\right] \qquad (3.4)$$

Where θ_1, θ_2 and θ_E are the optimum FAs and the Ernst angle, respectively, and $S(\theta_1)$, $S(\theta_2)$and $S(\theta_E)$ are the signals associated withθ_1, θ_2 and θ_E, respectively.

However, the two optimum FAs for maximizing (DR*FS) may not be the same as the pair of FAs for maximizing the contrast between GM and WM (CNR_{sub}). Chen et al suggested that the optimum pair of FAs for STAGE can be identified by maximizing the sum of CNR_{sub} and DR*FS. Figure 8 shows a 2D simulation plot of the described parameters. The ideal pair of FAs to achieve the best contrast between GM/WM (Figure 8. a) is $\theta_1 = 7°$ and $\theta_2 = 58°$, and the ideal pair of FAs to achieve higher precision DR*FS (Figure 8. b) is $\theta_1 = 10°$ and $\theta_2 = 50°$. Since an $\theta_1 = 10$ has a higher SNR than an $\theta_1 = 7°$ and an $\theta_2 = 50°$ has a lower specific absorption rate (SAR) than a $\theta_2 = 58°$, we used $\theta_1 = 10°$, $\theta_2 = 50$ for STAGE in our study (Figure 8. c).

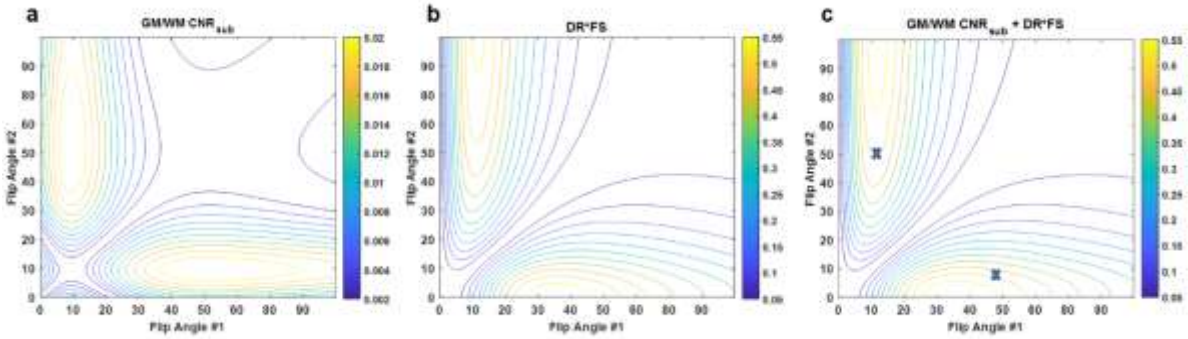

*Figure 7. 2D Contour plots of the **a)** CNR_{sub}, **b)** DR*FS and **c)** the sum of them. Each of the contours were plotted as a function of θ_1 and θ_2 to find the pair of FAs to maximize the contrast between gray matter and white matter and T1 precision. Optimal flip angles for producing the best maps were determined to be θ_1 =10º for the PD map and θ_2 =50º for the T1 map . Optimal choice of FAs was determined by cross in c part.*

The VFA derived map is susceptible to deviation from the correct value due to RF inhomogeneity or receive field (B_{1r} field variation) and non-uniformity of FA or receive field (B_{1t} field variation). Both B_{1r} and B_{1t} are location dependent. This may result in variation in signal intensity for a given tissue at different positions due to spatial variation. To consider these terms in the presence of RF field inhomogeneity, the spoiled gradient echo equation as a function of FA is given by:

$$S = PD * bias * \sin(k * \theta) * \frac{1 - E_1}{1 - \cos(k * \theta) * E_1} * e^{-\frac{TE}{T2^*}} \qquad (3.5)$$

Where k refers to the B_{1t} field variation and $bias$ refers to B_{1r} field variation. The equation (3.5) can be rewritten as:

$$\frac{S}{\sin(k*\theta)} = E_1 * \frac{S}{\tan(k*\theta)} + PD_{eff}(1-E_1) \quad (3.6)$$

Where

$$PD_{eff} = PD * bias * e^{-\frac{TE}{T2^*}} \quad (3.7)$$

By acquiring data for different nominal FAs, we can transform the data to fit a line with the slope of E_1 and $PD_{eff}(1-E_1)$ intercept. It should be noted that according to Deoni et al's study, two optimum FAs, the former of which is smaller than the Ernst angle and the latter is larger , are enough to map out a reliable T1 value; however, because of the B_{1t} field variation, the actual FAs may not be similar to the nominal FAs selected for mapping. This can cause significant error for T1 estimation especially at high field (>1.5T) (Weiskopf et al., 2011). To avoid aberration, prior information about B_{1t} is essential. Involving more data in the model improves the accuracy at the cost of increasing scan time.

Helms et al showed that the influence of k in FA miscalibration affects T1 and PD as in the following formula (Helms, Dathe, & Dechent, 2008):

$$PD_{app} = k * PD_{eff} \quad (3.8)$$

$$T_{1_{app}} = T_1 * k^2 \quad (3.9)$$

Where PD_{app} and $T_{1_{app}}$ are apparent values scaled by k and k^2 ,respectively. For example, 10% error in FA can lead to 10% in PD estimation and 20% in T1 estimation. STAGE proposed a novel method to extract B_{1t} and B_{1r} fields. However, in this study no RF transmit field effect, B1 correction wasn't applied for T1 mapping because of the low field used. The result of this assumption is validated with the phantom experiment.

Figure 9 shows the simulation of signal intensity for WM and GM for two optimum FAs as a function of k (equation (3.5)) with described parameters. The bias field in

equation (3.5) was ignored due to hardware manipulation corrections by the manufacturers. It is concluded that an FA smaller than the Ernst angle is more susceptible to deviation by B_{1t} field variation (k map). STAGE defined the T1WE image by means of the linear subtraction of the higher FA and corrected lower FA, which refers to finding a scale factor to make the lower FA signal value less sensitive to k variation. Consider the equation below:

$$S_{T1WE} = S'(\theta_2, TE_n) - \lambda S'(\theta_1, TE_n) \tag{3.10}$$

Where $\theta_1 = 10$, $\theta_2 = 50$ and $\lambda = \frac{1}{k^{\alpha}}$ which k represents B_{1t} field variation and α is constant value and equals 1.2 here. TE_n denotes n^{th}echo. Our scans are triple-echo scans, and the final T1WE is the average of the three T1WE images calculated from equation (7).

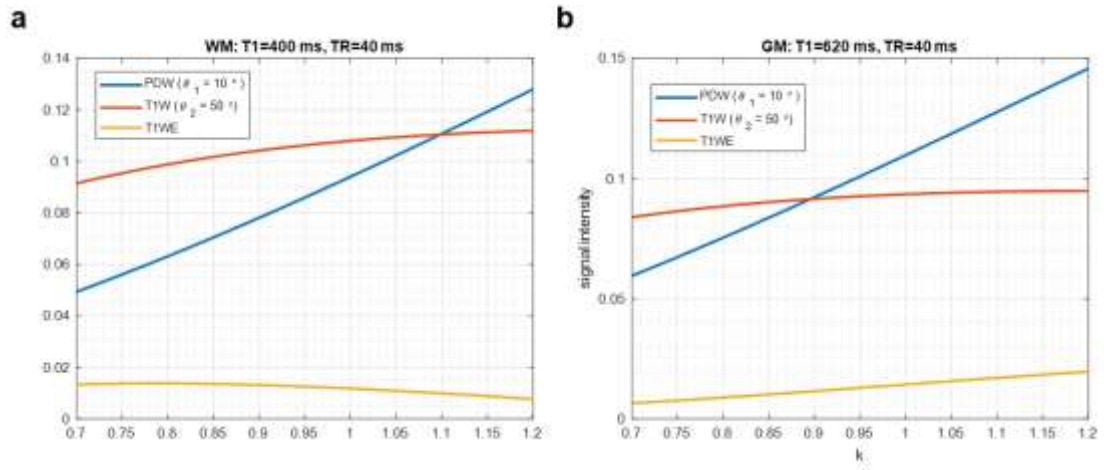

Figure 8. Spoiled gradient signal intensity as a function of k for a) WM and b) GM based on equation (3.5) and bias=1. For both GM and WM, the PDW suffers from more B1 field inhomogeneity than T1W, while T1WE has more uniform behavior.

3.1.3 In vivo data acquisition and processing

Simulations were performed to optimize the STAGE flip angles for the signal-to-noise ratio (SNR). Initial protocol development consisted of imaging healthy brain volunteers who consented to an institutional review board (IRB) study with a 12-channel flexible surface coil. Trade-offs between SNR, scan time, and spatial resolution for whole-brain coverage were evaluated. Two triple-echo spoiled gradient acquisitions at 1X1X3 mm^3 resolution were collected with a total acquisition time of 10

minutes. Weekly serial imaging was performed for a post-surgical glioblastoma case to demonstrate the feasibility of mapping changes with a Siemens 0.35T scanner coupled with a linear accelerator on the MRIdian Linac (ViewRay, Mountain View, CA) with imaging parameters described in Table 1.

Table 1. STAGE imaging protocol for in vivo experiment for 0.35T

Protocol	Axial PDW	Axial T1W
TR (ms)	40	40
TE (ms)	5.0/20.63/34.14	5.0/20.63/34.14
FA (deg)	10	50
BW (Hz/pixel)	100/100/100	100/100/100
Voxel Size	1.0*1.0*3.0	1.0*1.0*3.0
Flow Compensation	No/No/No	No/No/No
Acc. Factor (GRAPPA)	OFF	OFF
Slices	64	64
Acquisition Time (min:sec)	4:39	4:39

Despite the potential for STAGE producing QSM and SWI images, we did not use them in this study because of the limited echo time. For a tissue with specific susceptibility, the phase is proportional to B_0. Therefore, an echo time of 35 ms cannot provide sufficient contrast of phase images for a normal venous system, midbrain structures and basal ganglia structures. Figure 10shows the phase variation for demonstrated ROI. However, for patients with pathological lesions or cerebral microbleeds (CMBs), we may use this pseudo-SWIM (QSM) to identify whether there are any CMBs or hemorrhages inside a tumor, which could be a pure lesion map for high susceptibility lesions and CMBs.

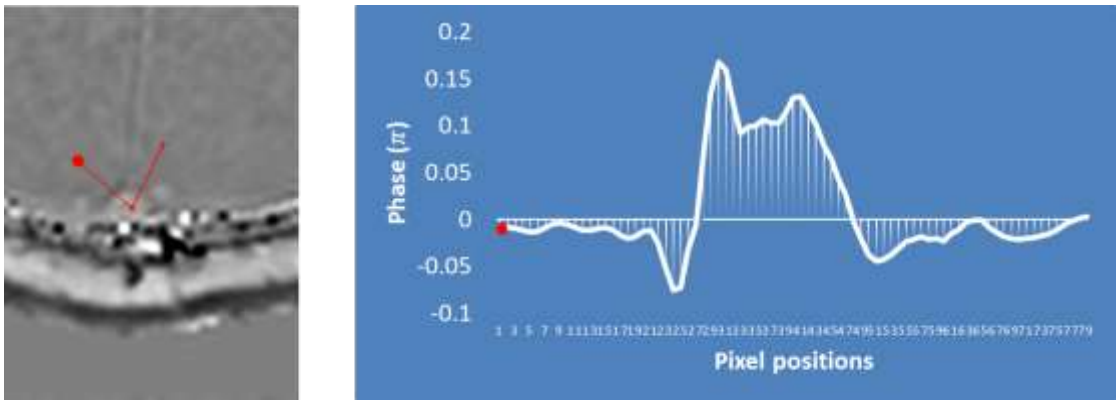

Figure 9. QSM (pseudo-SWIM) with TE=35ms shows relatively poor phase contrast due to intrinsic susceptibilities of the superior sagittal sinuses.

Figures 11 and 12 show STAGE implementation results on a healthy volunteer for slices 27 and 36 out 64, respectively (patient results will be discussed in the next chapter). PDW and T1W were original acquired images, while all other images/data were processed results. T1WE has better GM/WM contrast and better SNR than original T1W. Pseudo-SWIM was from the third echo of the PDW scan with TE=34.14ms. Simulated FLAIR was calculated from the quantified tissue properties with TR=10s, TE=15ms and TI=2200ms, which also can be done with different parameters for different image weighting and purposes.

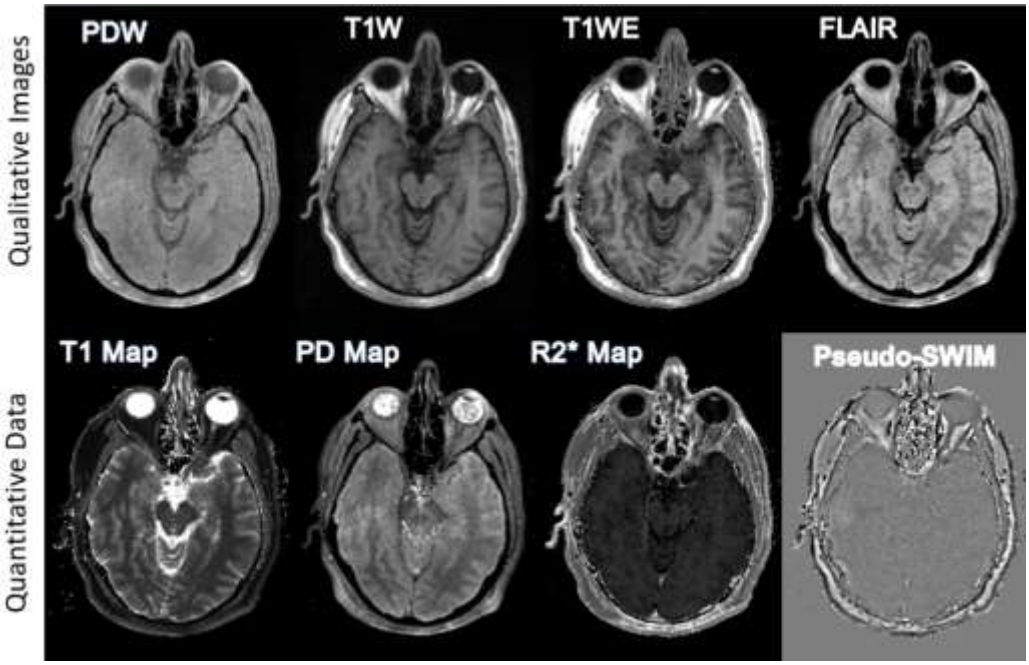

Figure 10. 10 min scans at 0.35T provided qualitative and quantitative images with a resolution of 1x1x3 mm^3 covering the whole brain. PDW and T1W were the original acquired images, while all other images/data were processed results. T1WE has better GM/WM contrast and better SNR than the original T1W. All images are slice 27 out of 64 for a healthy volunteer.

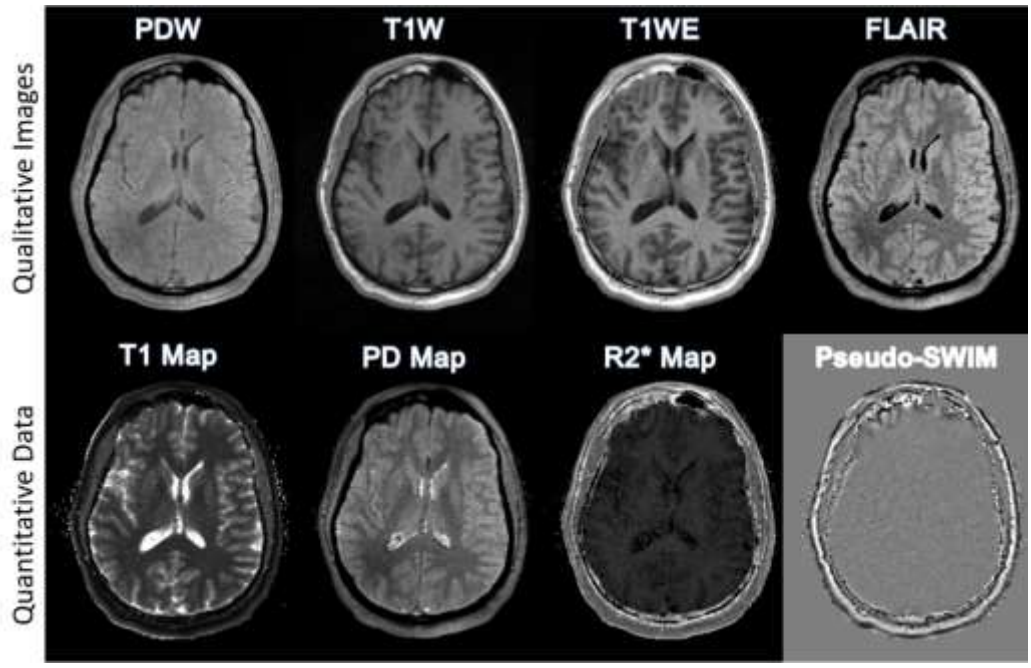

*Figure 11. T1WE, FLAIR, R2*MAP, T1MAP, and PDMAP were calculated from the two GRE scans using our STAGE software. Pseudo-SWIM was from the third echo of the PDW scan with TE=34.14ms. Simulated FLAIR was calculated from quantified tissue properties with TR=10s, TE=15ms and TI=2200ms, which also can be done with different parameters for different image weighting and purposes. All images are slice 27 out of 64 for a healthy volunteer.*

3.2 Phantom Benchmarking

An MRI system phantom has been developed through collaboration between the ISMRM ad-hoc committee on Standards for Quantitative Magnetic Resonance and the National Institute of Standards and Technology (NIST). This is the first phantom with an SI-traceable component. (https://collaborate.nist.gov/mriphantoms/bin/view/MriPhantoms/MRISystemPhantom).

The phantom includes a spherical shell with a 100mm inner radius which is filled with deionized water. There are 5 plates inside the phantom which are rigidly connected with positioning rods. There are 14 fiducial elements in a T1 array, 14 fiducial elements in T2 array, 14 fiducial elements in a PD array, 3 resolution insets (1 mm to 0.6 mm ± 0.015 mm) and (0.8 mm to 0.4 mm ± 0.015 mm), and 2 wedges at 10° for slice depiction. As Figure 13 demonstrates, the system is comprised of the following items:

- Plate 5: 4 fiducial spheres, serial number, system standard ID, T1 array (blue-green), resolution insets
- Plate 4: 13 fiducial spheres, T2 array (red), 2 resolution insets (1 mm to 0.06mm and 0.8 mm to 0.4 mm)
- Plate 3: 21 fiducial spheres, proton density array (yellow),
- Plate 2: 13 fiducial spheres, slice profile wedges
- Plate 1: 5 fiducial spheres (blue)

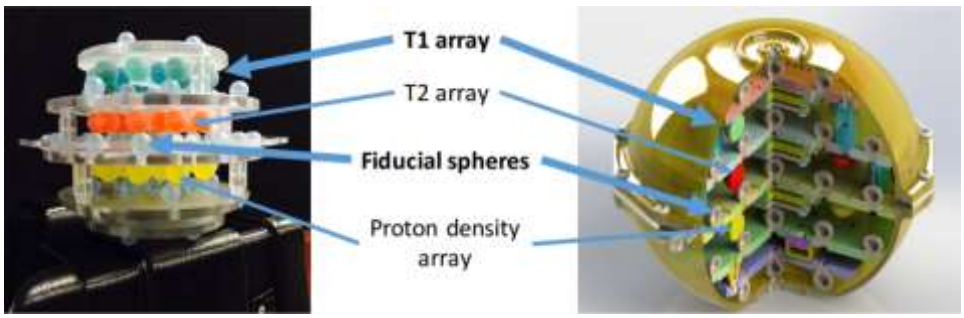

Figure 12. ISMRM/NIST phantom configuration

The 14 fiducial spheres in the T1, T2 and PD arrays have 10 ± 0.1 mm inter diameters fixed on a 3D 40 ± 0.1 mm grid. The origin of the phantom was designed at the center of the central fiducial sphere. The configuration was defined such that the plates are in the coronal plane with left, right superior, inferior designed on each plate. There is a notch placed in the mounting plate for convenient placement within the scanner. It is supposed that the configuration of the system standards mimic a human head with minimal distortion. Indeed, the orientation of the phantom should be the same as a patient lying supine on the imaging bed. Figure 14 illuminates a top view of the T1, T2 and PD plate. Note that all the spheres are the same in terms of size and the images are shown based on the plate size.

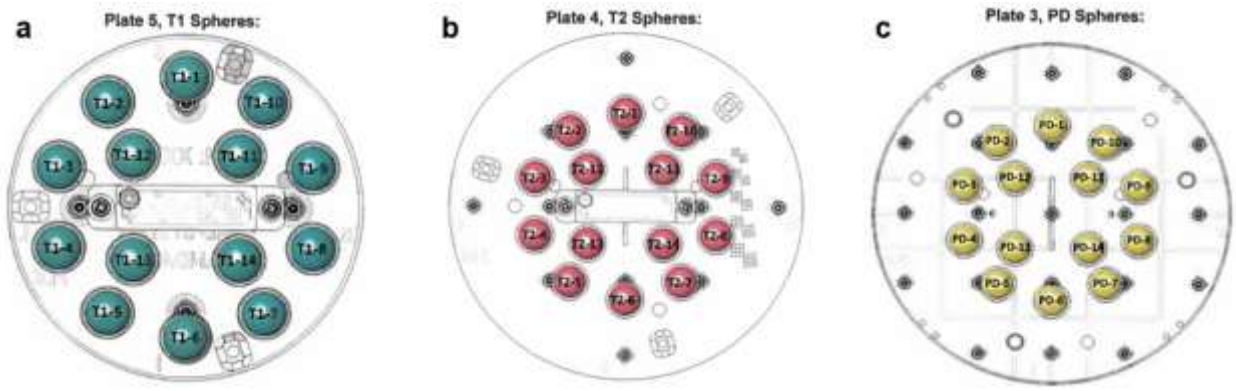

Figure 13. Axial view of three main arrays of ISMRM/NIST phantom a) T1 array b) T2 array c) PD array

The ISMRM/NIST phantom has multiple layers which are designed to have a wide range of T1, T2 and proton density values. The compartments of each layer have been characterized and monitored by NIST in terms of stability and accuracy (Russek, Boss, Jackson, Jennings, Evelhoch, Gunter, & Sorensen, 2012), (Jiang et al., 2017).

Several studies have been characterized using the ISMRM/NIST phantom for NMR relaxation time quantifications (Russek, Boss , Jackson, Jennings DL, Evelhoch & AG, 2012) and (K. Keenan et al., 2013). T1 variation assessed across multiple MRI systems and IR and VFA were compared in terms of precision (Keenan et al., 2013). For three vendors, IR and VFA were compared at 1.5T and 3T. It was observed at 3T that the repeatability of VFA may face systematic variation, approximately 20%. (Keenan et al., 2016)

Spheres in the T1 plate contained $NiCl_2$, and spheres in the T2 plate contained $MnCl_2$. It was proved that adoption of Ni^{2+} made theT1 value NMR frequency independent and relatively temperature independent (Kraft, Fatouros, Clarke, & Kishore, 1987). Indeed, reported values from the manufacturer for T1 at 1.5T and 3T can be used as a reference for our study in 0.35T.

3.2.1 Design imaging protocol for phantom experiment

In this study we used the ISMRM/NIST phantom to validate T1, R2* and the PD map which was accessible by conducting the STAGE sequence and post processing. This phantom study was designed to investigate the accuracy of T1, R2* and PD mapping without B1 correction at 0.35T to ensure whether it is clinically acceptable or not. The critical point for designing the phantom experiment was to select optimum FAs by considering a wide range of mapping values and having a reasonable SNR value.

To analyze accuracy, STAGE T1 map was compared with reported reference values by the manufacturer (the referenced values for 1.5T and 3T). As discussed, the phantom T1 value does not vary significantly over magnetic field strength, and it is stable as a function of temperature. In other words, it is relatively independent from field strength and temperature. Also, we ran an IR sequence to have a gold standard for comparison of the STAGE T1 map. In addition, there is a suggested imaging protocol for VFA according to the product manual of the phantom at 1.5T and 3T. The protocol was run to have an accurate method to compare. Since STAGE is designed based on the VFA, this gives the means for direct comparison.

The ISMRM/NIST phantom has 14 vials (spheres) in a T1 array. The 1st vial has the highest T1= 1879 at 1.5T and 1838 at 3T, and the 14th vial has the lowest T1= 24.19 at 1.5T and 22.95 at 3T. The choice of optimum FAs needs to consider critical points. The following algorithms were accomplished:

1. Simulation was performed to extract two optimum FAs for each vial.
2. The effect of noise and spoiled gradient signal linearity were investigated.

3. Based on the range of the FAs in the 1st and 2nd steps, the proper FAs were selected.

It was previously discussed that the signal of the spoiled gradient as a function of FA is given by:

$$S(\theta) = M_0 \sin\theta \frac{1 - E_1}{1 - \cos\theta * E_1} * e^{-\frac{TE}{T_2^*}} \quad (3.11)$$

That M_0 and T1 can be determined at multiple flip angles at a fixed TR. This equation can be rewritten as

$$\frac{S(\theta)}{\sin\theta} = E1 * \frac{S(\theta)}{\tan\theta} + M_0 * e^{-\frac{TE}{T_2^*}}(1 - E_1) \quad (3.12)$$

We can transform the points $(\theta, S(\theta))$ into a plane where the coordinate pairs are

$$(x(\theta), y(\theta)) \equiv (\frac{S(\theta)}{\tan\theta}, \frac{S(\theta)}{\sin\theta}) \quad (3.13)$$

This transforms the measured points into a straight line with slope E1 and the intercept of $M_0 * e^{-\frac{TE}{T_2^*}}(1 - E_1)$. Figure 15 illustrates the plots of the spoiled gradient signal verses θ and replots the same data in the transformed $(x(\theta), y(\theta))$ plane to highlight the linear form of the data in the transformed plane. If TE $\ll$ T2*, the exponential term of the intercept is negligible. Once the slope of the data E1 is determined by a linear least-square fit, T1 is known and M_0 is measurable by the intercept and T1 value.

In Figure 15, both parts are plotted based on the 5th vial of the ISMRM/NIST phantom with T1=527 ms and T2=457.5 ms. In (a), the last two points have deviations from the signal model in theory. This resonance offset increment makes the data not ideal. The failure of amplifiers in adjusting the signal at large flip angles is the possible reason for the misbehavior. In (b), the slope of the data indicates E1 and the intercept of $M_0 * e^{-\frac{TE}{T_2^*}}(1 - E_1)$ .The transformation of data shows that for small FAs, noise effects are more dominant. Selecting very small FAs may reduce noise propagation and SNR decrement.

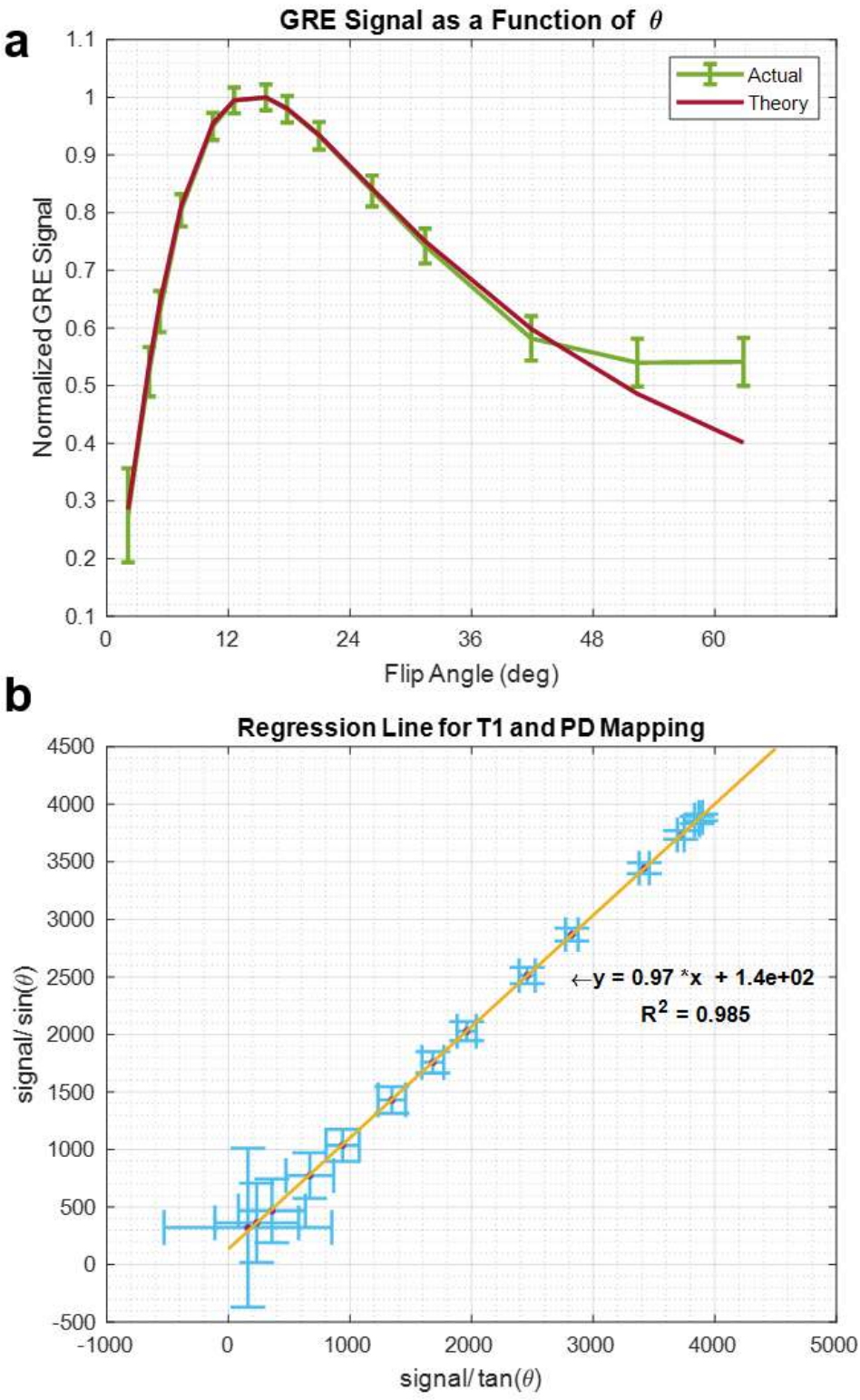

Figure 14. ***a)*** *Normalized spoiled gradient signal as FA based on equation (3.11) and signal from the scanner acquired from the 5th spheres on the T1 array with T1= 527. For FAs larger than 40°, the signal isn't fitted to the theoretical model, which leads to exclusion of large FA (>40°) for choice of optimum FAs for mapping.* ***b)*** *Replot of equation (3.11) to* $(x(\theta), y(\theta))$ *plane. Although in (a) error bars seem to have the same value, transformation to the mentioned plane shows that the noise effect for very small FA is more severe than the rest, which leads to exclusion of small FAs (≤ 4°) for phantom mapping.*

Figure 15 demonstrates that by eliminating small FAs, R^2 value and intercept was improved which is evident of selecting small FAs may lead to decrease in accuracy.

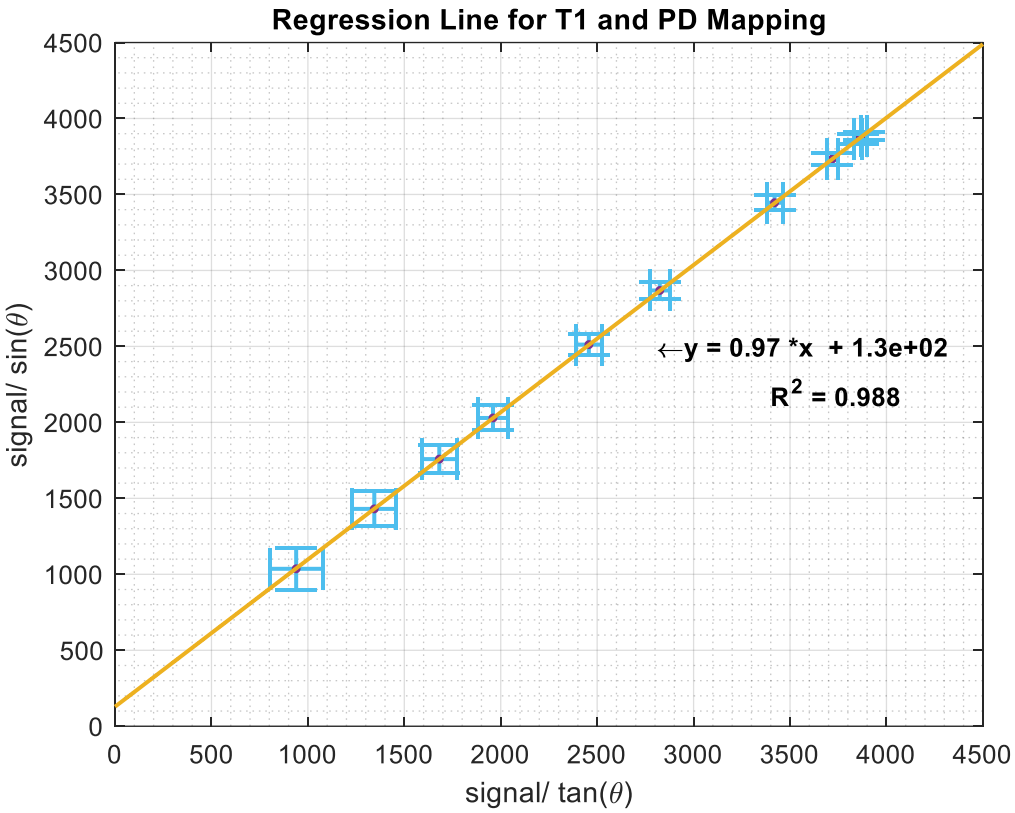

Figure 2. Improvement in accuracy by eliminating small FAs

3.2.2 Optimal Choice of FAs

In general, in optimization problems, the operating points should be selected such that the sensitivity of the measured quantity relative to the parameter of interest is maximized. Sensitivity is defined as the relative changes of the measured quantity in the case of the parameter variations. It measures how sensitive a signal/system is to an added disturbance in the parameter. Here, to estimate the T1 value, the choice of FAs should maximize the sensitivity of the measured signal relative to T1 to enhance SNR. Consider that the white noise ϵ_i (with standard deviation σ) is added to signal $S(\theta_i)$ so that $\sigma \ll S(\theta_i)$ for all of i. We have (Brown, Cheng, & Haacke, 2014):

$$\sigma_{T1}^2 = \sigma^2 \sum_i (\frac{\partial T1}{\partial S(\theta_i)})^2 \cong \sigma^2 \sum_i \frac{1}{(\frac{\partial S(\theta_i)}{\partial T1})^2} \qquad (3.14)$$

This indicates that by maximizing $\frac{\partial S(\theta_i)}{\partial T_1}$, the sensitivity of the signal to T1, the SNR will be boosted. Since for T1 mapping at an arbitrary FA the M_0 is necessary, the optimal choice of FAs includes selecting the pairs so that one of them has high sensitivity for T1 and the second has sensitivity for M_0. It has been shown that for $\theta \gg \theta_E$ the signal is T1 weighted and has high sensitivity to T1; it should be big enough to have high sensitivity and small enough to avoid offset problems as shown in Figure 15. On the other hand, for $\theta \ll \theta_E$ the signal is M_0 weighted and has high sensitivity to M_0; it should be small enough to have high sensitivity and large enough to have adequate SNR.

As discussed in the last chapter, Deoni et al suggested the following formula to estimate a pair of optimum FAs for T1 and M_0 mapping to maintain the mentioned criteria:

$$\theta = \cos^{-1}(\frac{f^2 E_1 \pm (1 - E_1^2)\sqrt{1 - f^2}}{1 - E_1^2(1 - f^2)}) \qquad (3.15)$$

Where f = 0.71.

Figure 16 shows the 2D contour plot for choosing the pair of FAs for the 6th vial and Table 2 expresses the pair of optimum FAs for each vial as well as Ernst angle. Ernst angle can be estimated by (Brown, Cheng, & Haacke, 2014)

$$\theta_E = \cos^{-1}(E_1) \sim \sqrt{\frac{2 * T_R}{T1}} \tag{3.16}$$

If θ_1 and θ_2 is the pair of the optimum FAs, and θ_E denotes the Ernst angle, the relation between them is

$$\frac{S(\theta_2)}{S(\theta_E)} = \frac{S(\theta_E)}{S(\theta_1)} \tag{3.17}$$

Where $S(\theta_1)$, $S(\theta_2)$ and $S(\theta_E)$ are the signal associated with θ_1, θ_2 and θ_E, respectively.

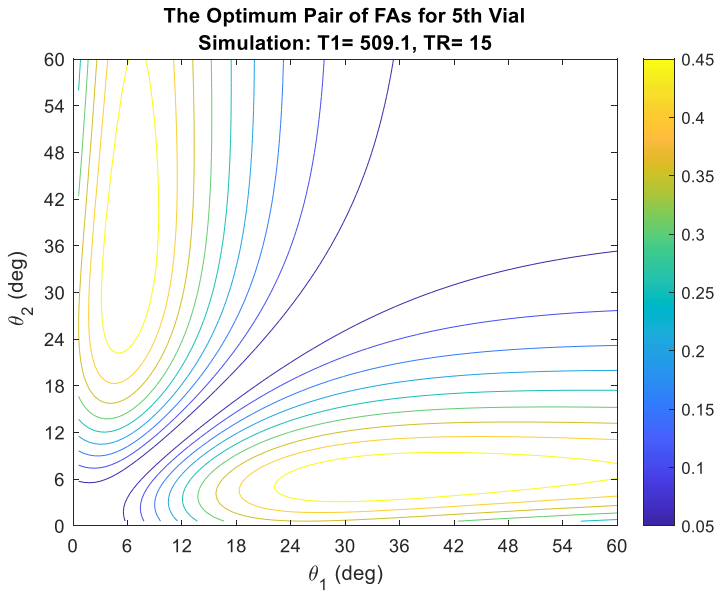

Figure 16. 2D contour plot for choice of the pair of FAs for the 6th vial

Table 2. The pair of optimum FAs for each vial as well as the Ernst angle

Spheres in T_1 Array (ms)	1st flip angle (deg)	2nd flip angle (deg)	Ernst angle (deg)
$\mathbf{1}\boldsymbol{st}$, $\mathbf{T_1 = 1838}$	3.04°	17.43°	7.31°
$\mathbf{2}\boldsymbol{nd}$, $\mathbf{T_1 = 1398}$	3.49°	19.94°	8.39°
$\mathbf{3}\boldsymbol{rd}$, $\mathbf{T_1 = 998.3}$	4.13°	23.50°	9.93°
$\mathbf{4}\boldsymbol{th}$, $\mathbf{T_1 = 725.8}$	4.85°	27.42°	11.64°
$\mathbf{5}\boldsymbol{th}$, $\mathbf{T_1 = 509.1}$	5.78°	32.48°	13.90°
$\mathbf{6}\boldsymbol{th}$, $\mathbf{T_1 = 367}$	6.81°	37.87°	16.38°
$\mathbf{7}\boldsymbol{th}$, $\mathbf{T_1 = 258.7}$	8.11°	44.45°	19.51°
$\mathbf{8}\boldsymbol{th}$, $\mathbf{T_1 = 184.7}$	9.59°	51.61°	23.09°
$\mathbf{9}\boldsymbol{th}$, $\mathbf{T_1 = 130.8}$	11.38°	59.75°	27.43°
$\mathbf{10}\boldsymbol{th}$, $\mathbf{T_1 = 90.9}$	13.63°	69.10°	32.91°
$\mathbf{11}\boldsymbol{th}$, $\mathbf{T_1 = 64.2}$	16.17°	78.60°	39.16°
$\mathbf{12}\boldsymbol{th}$, $\mathbf{T_1 = 46.28}$	18.96°	87.78°	46.13°
$\mathbf{13}\boldsymbol{th}$, $\mathbf{T_1 = 32.65}$	22.39°	97.50°	54.92°
$\mathbf{14}\boldsymbol{th}$, $\boldsymbol{T_1 = 22.95}$	26.34°	106.88°	65.50°

Discovering the relation between the number of selected FAs for mapping and SNR verifies the selection of enough FAs with high accuracy. Indeed, the multiple number of spoiled gradient scans at FAs (deg) = [2, 4, 5, 7, 10, 12, 15, 17, 20, 25, 30, 40, 50, 60] were acquired. The described method (equation 3.12) was applied on the two scans, and T1 and PD maps were found, and the process was repeated with 3,4, … 14 scans to unfold the relation between SNR of the T1 maps as a function of the number of FAs. Figure 17 shows that increasing the number of FA does not elevate the SNR necessarily. The result can be justified by considering the point that despite the fact that involving more FAs in the model enhances the precision, it may increase the noise level as well. There is a trade-off between the number of FAs and SNR. However, if the number of FAs is not sufficient, the results may not have accuracy in the acceptable clinical range.

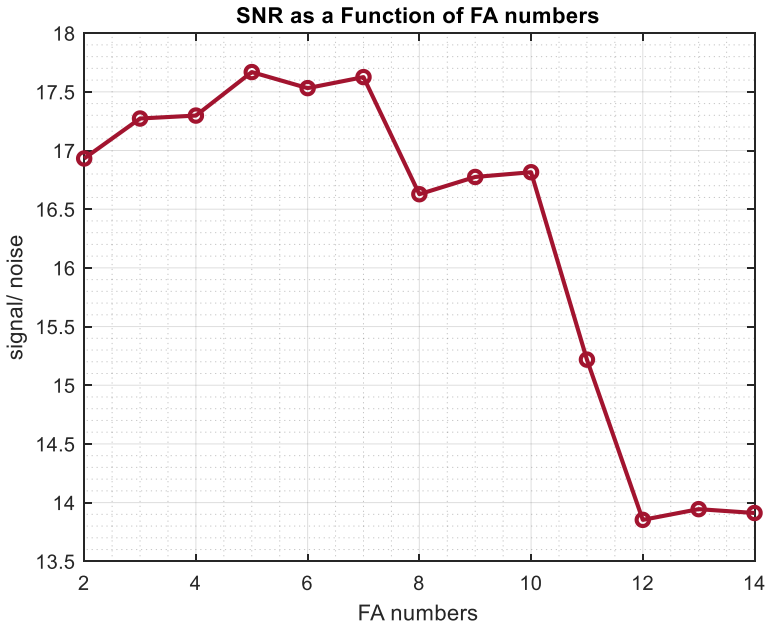

Figure 17. SNR as a function of the number of FAs for mapping through the VFA model

For selecting the optimum FAs for mapping, we prioritized the 5th vial in the T1 array, which has a similar T1 value for GM and WM at 0.35T. Also, we focused on the vial with T1> 60ms for mapping (the last three vials were excluded).

Three FAs were selected to be able to map 11 vials with the highest T1= 1838 ms lowest T1= 64.2 ms. Figure 17 ensures that involving 3 FAs results in reasonable SNR.

Initiating 7 FAs has the best SNR; however, in comparison to 3 FAs, it does not elevate the SNR much while it increases the scan time substantially. Indeed FAs (deg) = [5, 17, 32] were selected for the phantom experiment. The result will be justified in the next chapter.

Chapter References

Bottomley, P. A., Foster, T. H., Argersinger, R. E., & Pfeifer, L. M. (1984). A review of normal tissue hydrogen NMR relaxation times and relaxation mechanisms from 1-100 MHz: dependence on tissue type, NMR frequency, temperature, species, excision, and age. *Medical Physics*, *11*(4), 425–448. https://doi.org/10.1118/1.595535

Brown, R., Cheng, Y., & Haacke, E. (2014). *Magnetic Resonance Imaging: Physical Properties and Sequence Design* (2nd Editio). Retrieved from https://onlinelibrary.wiley.com/doi/book/10.1002/9781118633953

Chen, Y., Liu, S., Wang, Y., Kang, Y., & Haacke, E. M. (2018). STrategically Acquired Gradient Echo (STAGE) imaging, part I: Creating enhanced T1 contrast and standardized susceptibility weighted imaging and quantitative susceptibility mapping. *Magnetic Resonance Imaging*, *46*, 130–139. https://doi.org/10.1016/j.mri.2017.10.005

Deoni, S. C. L., Rutt, B. K., & Peters, T. M. (2003). Rapid combined T1 and T2 mapping using gradient recalled acquisition in the steady state. *Magnetic Resonance in Medicine*, *49*(3), 515–526. https://doi.org/10.1002/mrm.10407

Gupta, R. K. (1977). A new look at the method of variable nutation angle for the measurement of spin-lattice relaxation times using fourier transform NMR. *Journal of Magnetic Resonance (1969)*, *25*(1), 231–235. https://doi.org/https://doi.org/10.1016/0022-2364(77)90138-X

Helms, G., Dathe, H., & Dechent, P. (2008). Quantitative FLASH MRI at 3T using a rational approximation of the Ernst equation. *Magnetic Resonance in Medicine*, *59*(3), 667–672. https://doi.org/10.1002/mrm.21542

Jiang, Y., Ma, D., Keenan, K. E., Stupic, K. F., Gulani, V., & Griswold, M. A. (2017). Repeatability of magnetic resonance fingerprinting T1 and T2 estimates assessed using the ISMRM/NIST MRI system phantom. *Magnetic Resonance in Medicine*, *78*(4), 1452–1457. https://doi.org/10.1002/mrm.26509

Keenan, K., Boos, M., Jackson, E. F., Kown, S.-J., Jennings, D., & Russek, S. (2013). NIST/ISMRM MRI System Phantom T1 Measurements on Multiple MRI

System. *Proceedings 21st Scientific Meeting, International Society for Magnetic Resonance in Medicine*, *21*, 4338. Retrieved from http://collaborate.nist.gov/mriphantoms/bin/view/MriPhantoms/

Keenan, K. E., Stupic, K. F., Boss, M. A., Russek, S. E., Chenevert, T. L., Prasad, P., … Jackson, E. (2016). Comparison of T1 measurement using ISMRM / NIST phantom comparison of T1 measurement using ISMRM / NIST system phantom. *ISMRM 24th Annual Meeting, Singapore, 2016.*

Kraft, K. A., Fatouros, P. P., Clarke, G. D., & Kishore, P. R. (1987). An MRI phantom material for quantitative relaxometry. *Magnetic Resonance in Medicine*, *5*(6), 555–562.

Russek SE, Boss M, Jackson EF, Jennings DL, Evelhoch JL, G. J., & AG, S. (2012). Characterization of NIST/ISMRM MRI System Ph hantom. *Characterization of NIST/ISMRM MRI System Phantom. In Proceedings of the 20th Annual Meeting of ISMRM, Melbourne, Australia*, *20*, 2456. Retrieved from http://archive.ismrm.org/2012/2456.html

Venkatesan, R., Lin, W., & Haacke, E. M. (1998). Accurate determination of spin-density and T1 in the presence of RF-field inhomogeneities and flip-angle miscalibration. *Magnetic Resonance in Medicine*, *40*(4), 592–602.

Wang, Y., Chen, Y., Wu, D., Wang, Y., Sethi, S. K., Yang, G., … Haacke, E. M. (2018). STrategically Acquired Gradient Echo (STAGE) imaging, part II: Correcting for RF inhomogeneities in estimating T1 and proton density. *Magnetic Resonance Imaging*, *46*, 140–150. https://doi.org/https://doi.org/10.1016/j.mri.2017.10.006

Weiskopf, N., Lutti, A., Helms, G., Novak, M., Ashburner, J., & Hutton, C. (2011). Unified segmentation based correction of R1 brain maps for RF transmit field inhomogeneities (UNICORT). *NeuroImage*, *54*(3), 2116–2124. https://doi.org/10.1016/j.neuroimage.2010.10.023

Chapter 4

Main Findings, Results and Discussion

Introduction

This chapter has two sections: the phantom results and in vivo patient results. In the former, STAGE quantitative maps are critically evaluated and agreement with previous literature is discussed. In the latter, patient results are discussed, and serial data suggests the potential for monitoring tumor and tissue response for cancer patients undergoing MRgRT.

4.1 The Phantom Result

In this part, all of the STAGE quantitative maps including T1, PD and R2* are analyzed. The ISMRM/NIST phantom (SN: 0088) was placed into the magnet with the standard position. STAGE sequence was run using the 6-channel surface coil on the ViewRay/Siemens 0.35T system. The protocol includes three triple-echo GRE with FA=5^{o}, FA=17^{o} and FA=32^{o}, 1 x 1x 3 mm^{3} resolution, TR=40 ms, TE =5/20/34 ms. The total acquisition time was 14 minutes. The phantom benchmarking was characterized into intra-sessions and inter-sessions. The former included 6 consecutive scans, and the latter involved 5 scans on multiple days. It's expected that the maps with intra sessions acquisition have more accuracy than maps with intea sessions. This claim can be justified by the position of the coils. In intra sessions, coils are the same distance as phantom which gives more consistent signal.

4.1.1 STAGE T1 map result

Figure 18 shows the phantom configuration within the coils and T1 and R1 map. Reasonable agreement between STAGE low-field T1 mapping and references T1 values at 1.5T and 3T and IR were observed. For spheres # 1~ 11 (T1> 60 ms), the measured T1 errors (mean $\pm$ SD) with respect to those NMR references from 3T and 1.5T were 4.59% ± 1.62% and 7.64% ± 3.60% for intra-sessions and 13.38% ± 3.77% and 9.05% ± 3.51% for inter-sessions, respectively.

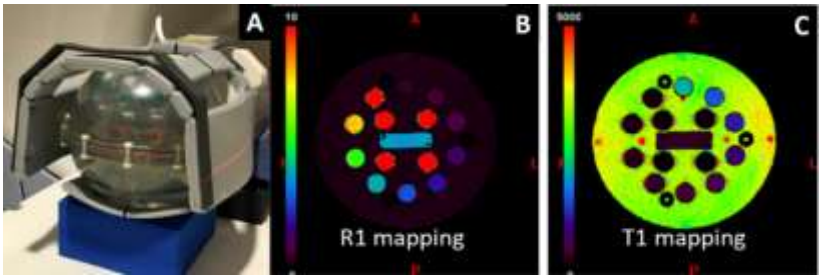

Figure 18. ***A)*** *ISMRM/NIST phantom in prototype head coil scanned at 0.35T. Results for T1 mapping verification including* ***(B)*** *R1 map,* ***(C)*** *T1 map*

Several studies have been characterized using the ISMRM/NIST phantom for NMR relaxation time quantifications (Russek, Boss, Jackson, Jennings, Evelhoch & AG, 2012) and (Keenan et al., 2013). The T1 variation assessed across multiple MRI systems and IR and VFA were compared r in terms of precision (Keenan et al., 2013). For three vendors, IR and VFA were compared at 1.5T and 3T. It was observed at 3T, so the repeatability of VFA may be susceptible to systematic variation, approximately 20%. (Keenan et al., 2016)

Sequence types, protocol and vendors may provoke systematic offset in T1 relaxation time measurement. B1+ field variations could contribute to systematic error. For our low field system, B1+ field variations were negligible. Despite the vulnerability of VFA to systematic offset, our STAGE T1 map had excellent agreement with the references. These results suggest that quantitative MRI at 0.35T is feasible. In the following, figures and tables are given for more details.

For intra-sessions:

Table 3 reports the STAGE T1 map, the T1 map from VFA with the suggested protocol from the phantom manual, the IR with TR/TE=5000ms/10ms, bandwidth=227Hz/pixel, 0.97x0.97x6mm^3, TIs (ms) = {0, 25, 50, 70, 100, 150, 200, 300, 500, 800, 1000, 1500, 2000, 2500} and reference values at 1.5T and 3T. The reported values are based on 50 pixels' ROI for all spheres.

Figure 19 is the corresponding plot of Table 3. Figures 20 and 21 plot the STAGE T1 map over NMR references from 3T and 1.5T to emphasize the ignorable systematic offset.

For inter-sessions:

Table 4 reports the STAGE T1 map, the T1 map from VFA with the suggested protocol from the phantom manual, the IR with the described parameters and reference values at 1.5T and 3T. Figure 22 is the corresponding plot of Table 4. The reported values are based on 50 pixels' ROI for all spheres.

Figures 23 and 24 indicate STAGE T1 map over NMR references from 3T and 1.5T to emphasize on ignorable systematic offset.

Table 3. STAGE T1 map acquired by averaging of six intra session acquisitions as well as IR and reference values at 1.5T and 3T. Uncertainties indicate white noise of the measuring. Uncertainties for ROI aren't shown here.

Num	STAGE T1 value (ms)	VFA T1 value (ms)	IR (ms)	1.5T (ms)	3T (ms)
1	1946.4 ± 132.9	1998.6 ± 169.1	2156.8	1879	1838
2	1378.6 ± 78.2	1466.3 ± 90.1	1521.5	1432	1398
3	969.6 ± 59.3	1058.1 ± 40.8	1025.3	1027	998.3
4	680.2 ± 49.0	751.7 ± 26.2	766.1	751.3	725.3
5	482.9 ± 27.2	509.1 ± 18.6	531.5	527	509.1
6	348.5 ± 20.2	353.4 ± 13.4	388.7	384.1	367
7	243.8 ± 13.8	252.0 ± 8.0	273.5	272.3	258.7
8	173.8 ± 16.0	185.9 ± 5.1	200.3	194.5	184.7
9	125.1 ± 13.5	126.8 ± 3.4	139.9	137.8	130.8
10	88.5 ± 8.1	87.2 ± 3.9	97.5	94.7	90.9
11	66.6 ± 9.82	62.3 ± 3.4	68.9	67	64.2

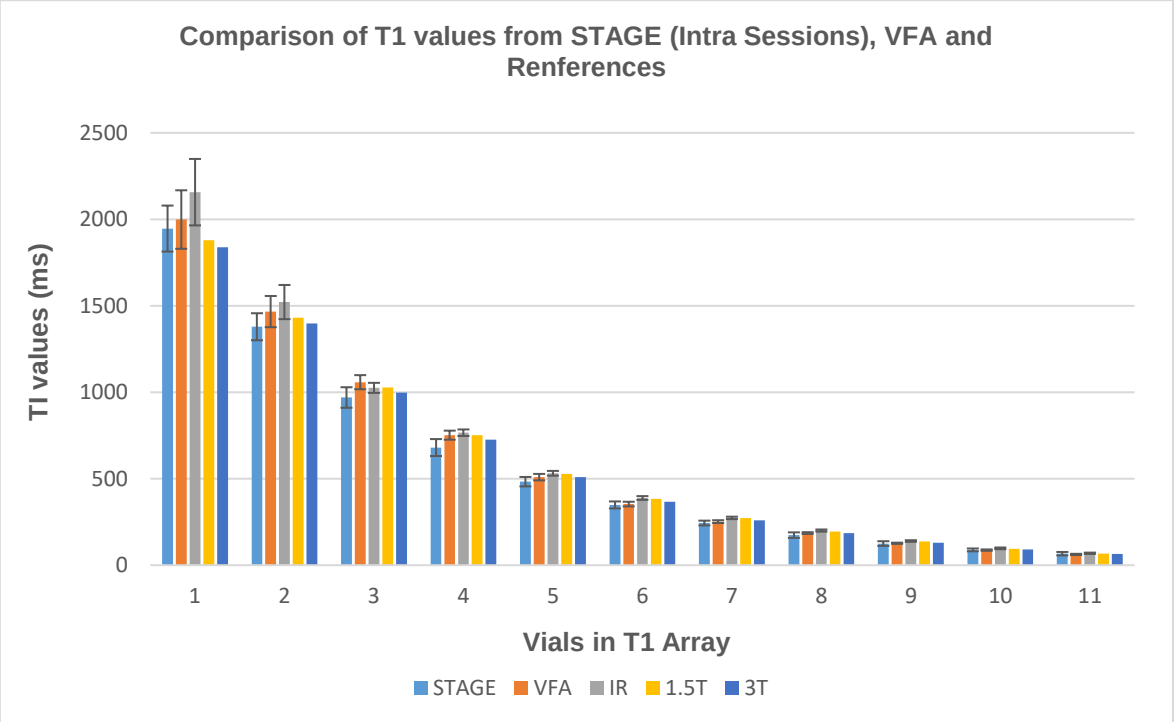

Figure 19. A comparison of STAGE T1 map acquired by averaging of six intra session acquisitions, VFA, IR and reference values at 1.5T and 3T. This figure is plotted based on Table 3 values. For spheres # 1~ 11 (T1> 60 ms), measured T1 errors (mean ± SD) with respect to those NMR references from 3T and 1.5T were 4.59% ± 1.62% and 7.64% ± 3.60 for intra-sessions, respectively.

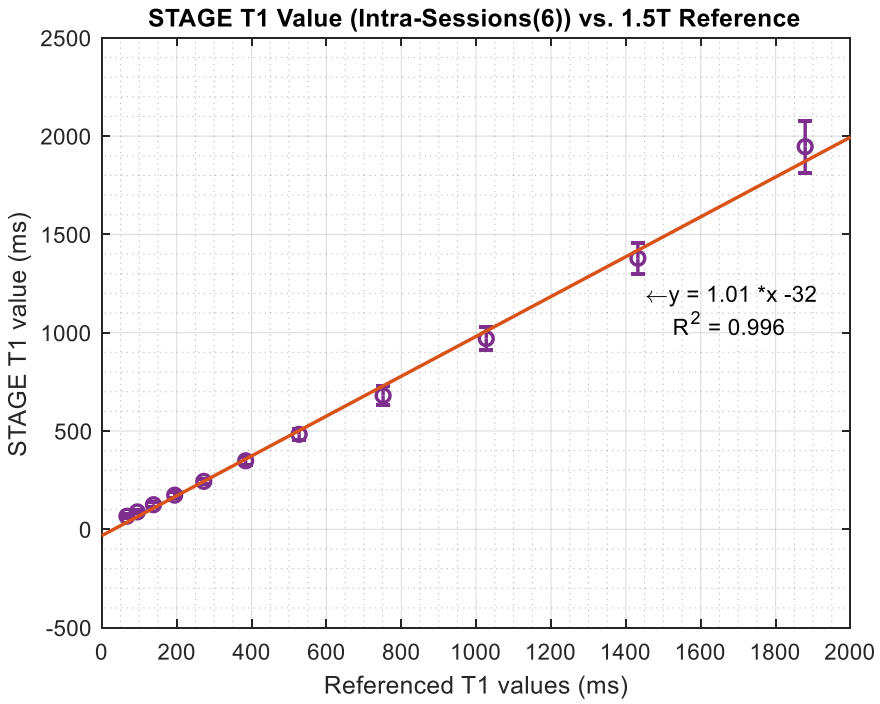

Figure 20. Measured STAGE T1 value acquired by averaging of six intra session acquisitions, over the referenced T1 value at 1.5 T. The slope of the regression line is an indication of agreement, which is close to 1. R^2 >0.99 confirms the authenticity of the approach. This strong agreement suggests the offset effect is negligible for our method.

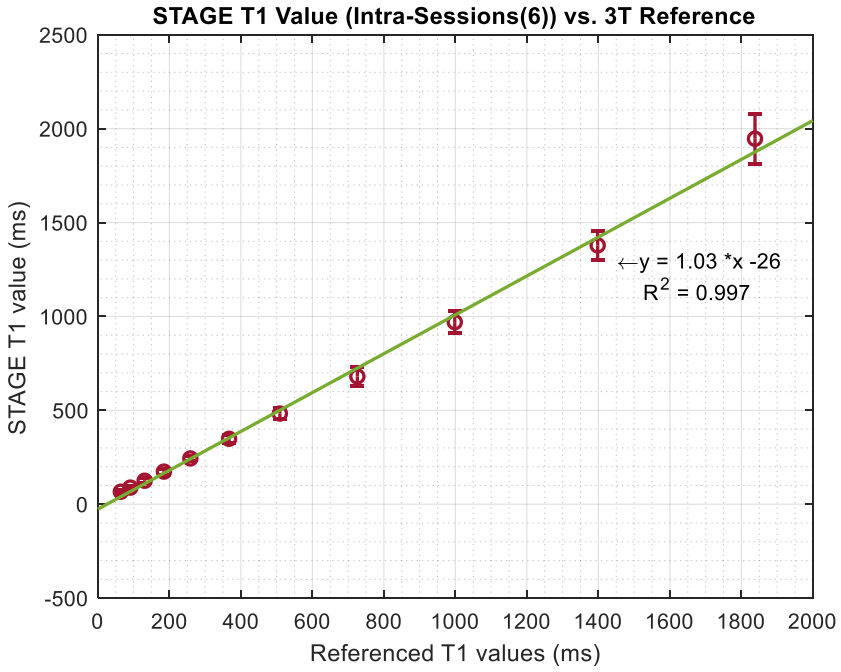

Figure 21. Measured STAGE T1 value acquired by averaging of six intra session acquisitions, over referenced T1 value at 3 T. The slope of the regression line is an indication of agreement, which is close to 1. R^2 >0.99 confirms the authenticity of the approach. The strong agreement suggests offset effect is negligible for our method.

Table 4. STAGE T1 map acquired by averaging of five inter session acquisitions, as well as IR and reference values at 1.5T and 3. Uncertainties indicate white noise of the measuring. Uncertainties for ROI aren't shown here.

Num	STAGE T1 value (ms)	VFA T1 value (ms)	IR (ms)	1.5T (ms)	3T (ms)
1	1785.4 ± 136.7	1998.6 ± 169.1	2156.8	1879	1838
2	1261.0 ± 74.1	1466.3 ± 90.1	1521.5	1432	1398
3	884.4 ± 65.5	1058.1 ± 40.8	1025.3	1027	998.3
4	632.0 ± 47.1	751.7 ± 26.2	766.1	751.3	725.3
5	464.6 ± 30.8	509.1 ± 18.6	531.5	527	509.1
6	343.4 ± 24.0	353.4 ± 13.4	388.7	384.1	367
7	235.0 ± 18.6	252.0 ± 8.0	273.5	272.3	258.7
8	170.0 ± 18.62	185.9 ± 5.1	200.3	194.5	184.7
9	119.8 ± 13.13	126.8 ± 3.4	139.9	137.8	130.8
10	81.9 ± 8.4	87.2 ± 3.9	97.5	94.7	90.9
11	62.3 ± 9.6	62.3 ± 3.4	68.9	67	64.2

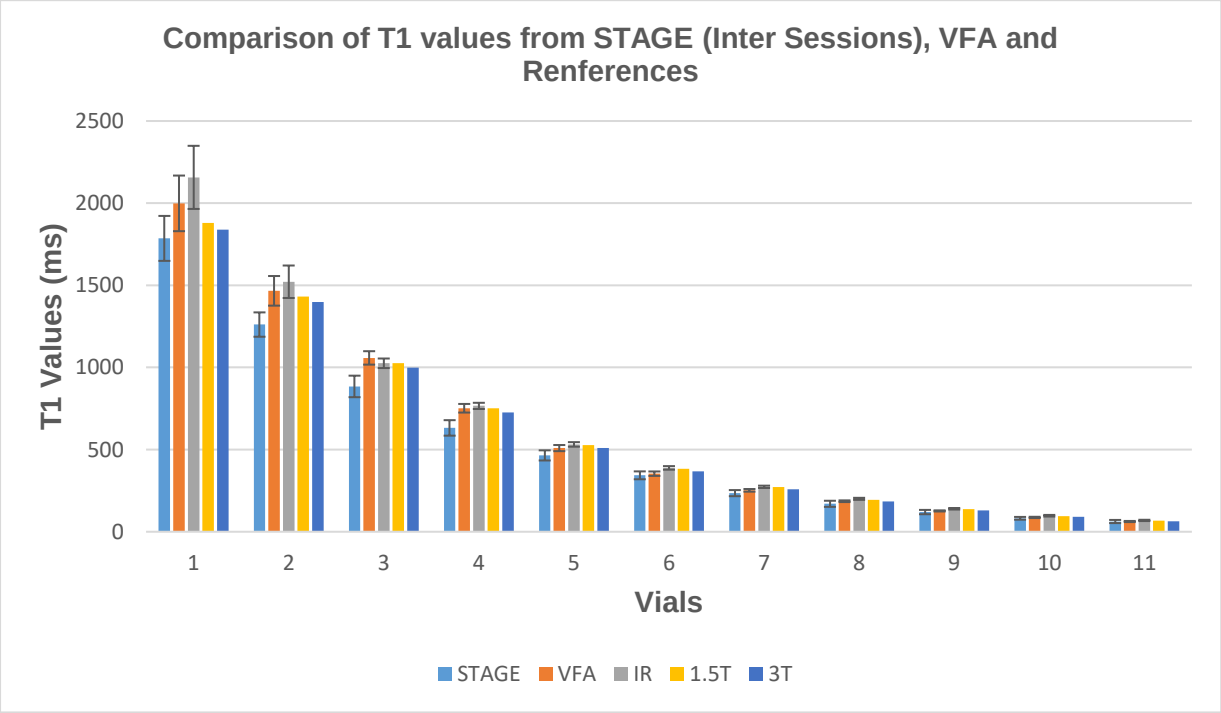

Figure 22. A comparison on STAGE T1 map acquired by averaging of five inter session acquisitions, VFA, IR and reference values at 1.5T and 3T. This figure is plotted based on Table 4 values. For spheres # 1~ 11 (T1> 60 ms), measured T1 errors (mean ± SD) with respect to those NMR references from 3T and 1.5T were 13.38% ± 3.77% and 9.05% ± 3.51% for inter-sessions, respectively.

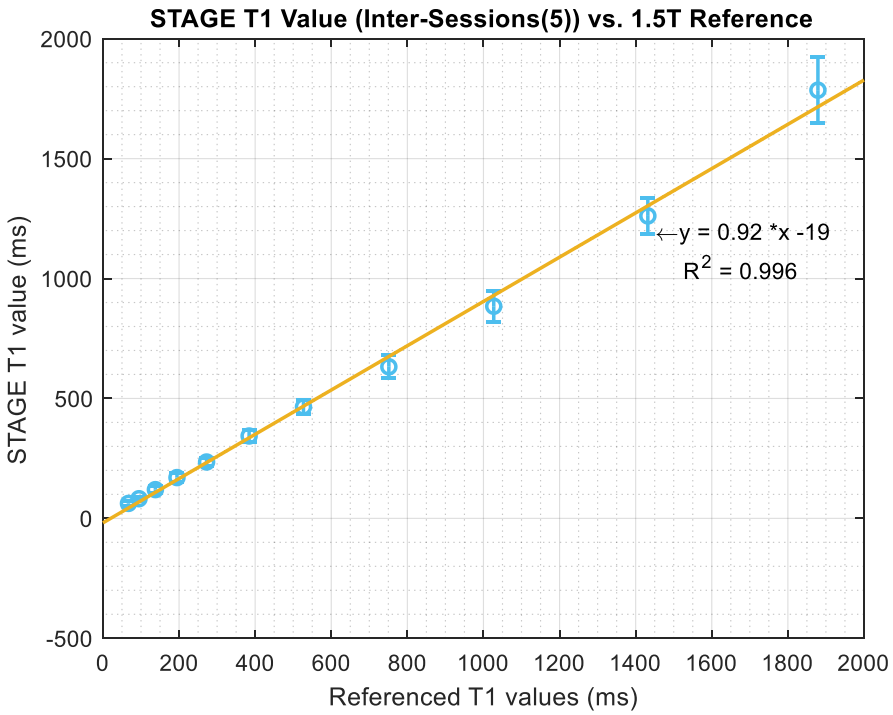

Figure 23. Measured STAGE T1 value acquired by averaging of five inter session acquisitions, over referenced T1 value at 1.5 T. The slope of the regression line is an indication of agreement, which is close to 1. $R^2 > 0.99$ confirms the authenticity of the approach. The strong agreement suggests offset effect is negligible for our method.

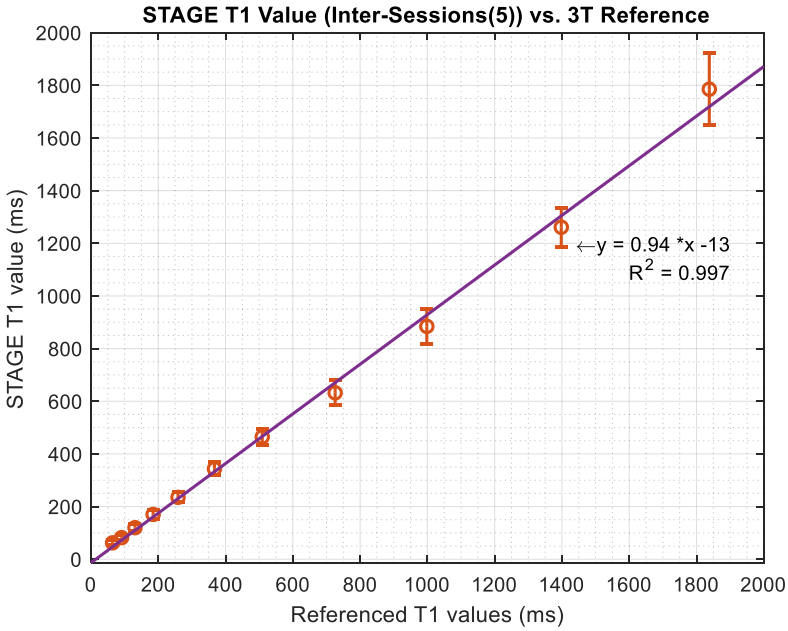

Figure 24. Measured STAGE T1 value acquired by averaging of five inter session acquisitions, over referenced T1 value at 1.5 T The slope of the regression line is an indication of agreement, which is close to 1. R2 > 0.99 confirms the authenticity of the approach. The strong agreement suggests offset effect is negligible for our method .

4.1.2 STAGE PD Map Results

Proton density refers to the concentration of protons that contribute to a tissue's signal. It is expressed as a percentage of the proton concentration in water in a percentage unit (pu). For example, CSF is 100 pu, WM is roughly 70 pu, and GM is 80 pu. In fact, all images have a PD-weighted effect as well as other possible parameter effects.

A reasonable way to assess PD is to determine water content; however, actual PD is slightly different. A significant number of protons are in a non-water environment (e.g. lipids). However, most of these components have short T2 and are not MR-visible. Their effects are negligible, especially in the brain, since most protons with long T2 (mobile protons) are in the water and are MR-detectable. PD is often approximately the same as the mobile water content of tissue (Tofts, 2014).

For phantom benchmarking, the relation between the STADE PD value and percent of water concentration of spheres in the PD plate is investigated. For both intra-session and inter-session experiments, the value of the STAGE PD map is proportional to the percent of water concentration (from the manufacturers).

Table 5 and Figure 25 are associated with intra-session experiments. Table 5 shows the STAGE PD map and the percent of nominal water concentration ,and Figure 25 shows agreements of the measured value with corresponding water concentrations.

shows the STAGE PD map and the percent of nominal water concentration , and Figure 26 indicates consensus between the measured value and the corresponding water concentrations.

Table 5. STAGE PD map value acquired by averaging of six intra session acquisitions for all spheres in PD array for intra-sessions. The sphere nominal water concentration is considered as a reference for validation.

Spheres	Nominal Water Concentration (%)	STAGE PD Value
1	5	11.23 ± 0.84
2	10	14.23 ± 1.04
3	15	18.96 ± 1.99
4	20	25.34 ± 0.49
5	25	27.47 ± 0.79
6	30	32.42 ± 0.78
7	35	37.27 ± 0.70
8	40	41.88 ± 0.79
9	50	51.94 ± 0.46
10	60	60.57 ± 0.48
11	70	69.41 ± 0.35
12	80	80.75 ± 0.88
13	90	88.88 ± 0.38
14	100	100.01 ± 0.20

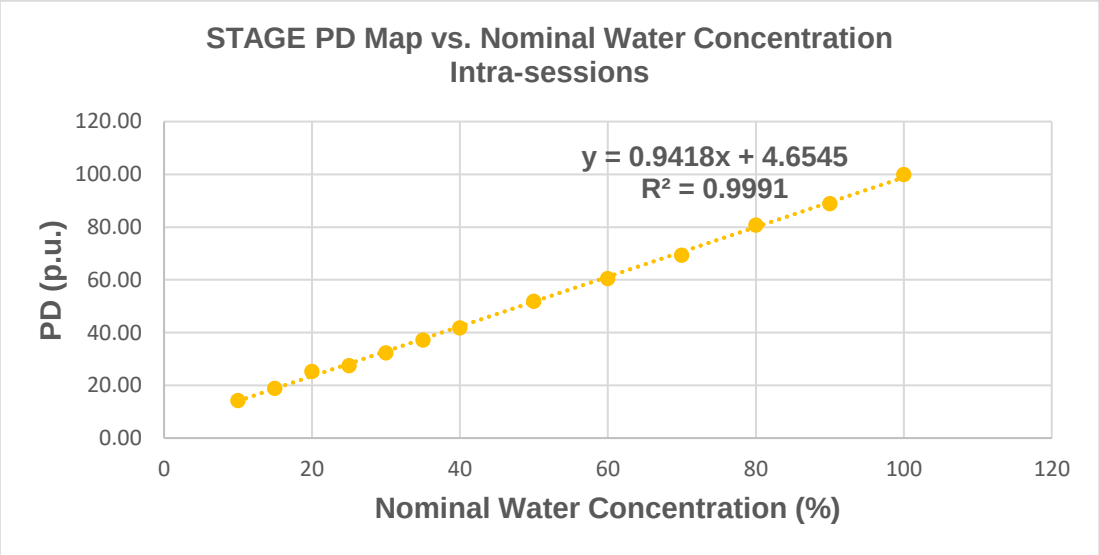

Figure 25. Measured PD value from STAGE acquired by averaging of six intra session acquisitions, as a function of nominal water concentration. The linear relationship indicates that the relative PD map is valid.

Table 6. STAGE PD map value acquired by averaging of five inter session acquisitions, for all spheres in PD array for inter-sessions. The sphere nominal water concentration is considered as a reference for validation.

Spheres	Nominal Water Concentration (%)	STAGE PD Value
1	5	11.80 ± 0.63
2	10	14.55 ± 0.23
3	15	20.10 ± 0.15
4	20	29.64 ± 0.46
5	25	31.22 ± 0.39
6	30	33.30 ± 0.32
7	35	38.38 ± 0.22
8	40	40.95 ± 0.17
9	50	49.82 ± 0.11
10	60	56.57 ± 0.19
11	70	68.03 ± 0.41
12	80	79.54 ± 0.19
13	90	92.85 ± 0.43
14	100	100.02 ± 0.20

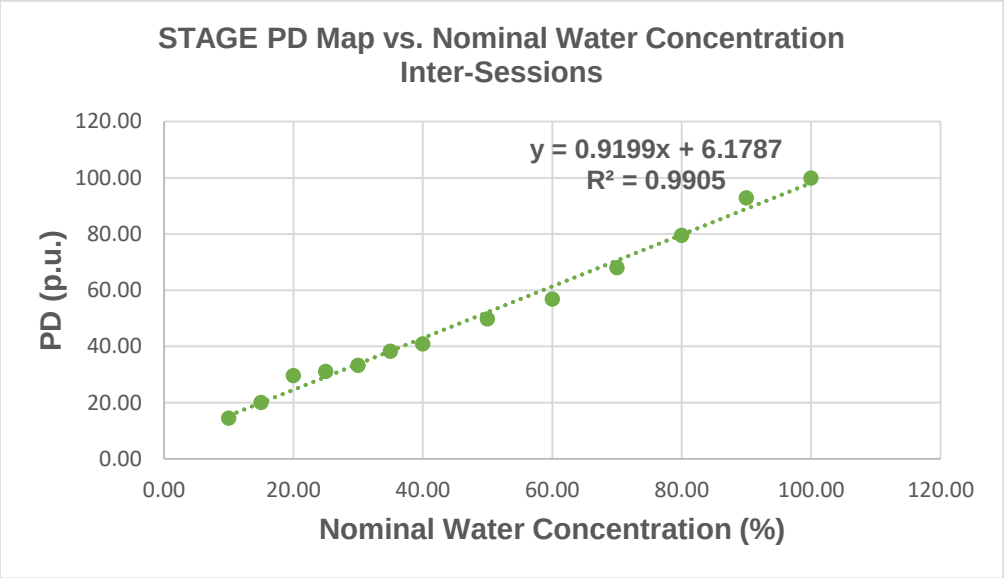

Figure 26. Measured PD value from STAGE acquired by averaging of five inter session acquisitions, as a function of nominal water concentration. The linear relationship indicates that the relative PD map is valid.

4.1.3 STAGE R2* Map Results

A quantitative T2* map is usually based on the exponential fitting of multi echo spoiled gradient sequence data or Carr-Purcell-Meiboom-Gill sequences (Chen & Qiu, 2018). If TE1 and TE2 are the first and second echo of the spoiled gradient sequence and S_1 and S_2 are the corresponding signals at that moment, T2* can be found by:

$$T_2^* = \frac{TE2 - TE1}{\ln(\frac{S_1}{S_2})} \Longrightarrow R_2^* = \frac{1}{T_2^*} \qquad (4.1)$$

Equation (4.1) highlights independence of T_2^* to bias field variation. This feature is critical at high field (> 3T).

The choice of TE times is critical in terms of SNR efficiency. The SNR can be found from

$$\frac{\sigma_{R2^*}}{R2^*} \propto \sqrt{2}\frac{\sigma_{T2^*}}{\Delta TE} \qquad (4.2)$$

If TE is selected smaller than T_2^*, tissues with long T_2^* may suffer from poor contrast. This point is considered in selecting third echo time for STAGE protocol.

SNR can be improved by averaging neighbor pixels. For example, if an image with $m * m$ pixel size is replaced with an image with $n * n$ pixel size by averaging neighbor pixels ($m > n$), SNR with improved by $\frac{m}{n}$

Most of the clinical studies for T2* were conducted at relatively high fields. In this study, by using two triple echo spoiled gradient sequences and fitting the data to a mono-exponential signal decay model, T2* is accessible. In the phantom experiment, an ISMRM/NIST phantom with various T2* values were used to assess the curve fitting model in low fields. The results show an excellent linear relationship between $MnCl_2$ and R2* value, which is an indication of the stability of accurate mapping (Chen & Qiu, 2018). This study closely matches in terms of linear relation parameters with the study at the same magnetic field strength (Chen & Qiu, 2018).

Table 7 and Figure 27 are associated with the intra-session experiment. Table 7 reveals the STAGE R2* map and the percent of nominal $MnCl_2$ concentration, and

Figure 27 shows agreement between the measured value and the corresponding $MnCl_2$ concentration.

Table 8 and Figure 28 correspond to the inter-session experiments. Table 8 demonstrate the STAGE R2* map and percent of nominal $MnCl_2$ concentration , and Figure 28 indicates a consensus in the measured value with the corresponding $MnCl_2$ concentration.

Table 7. STAGE R2 map value acquired by averaging of six intra session acquisitions, for all spheres in T2 array for intra-sessions. The spheres nominal $MnCl_2$ concentration is considered as a reference for validation.*

Spheres	$MnCl_2$ Concentration (±5%, mM)	STAGE R_2^* (1/s)
1	0.013	0.00162 ± 0.00107
2	0.021	0.00152 ± 0.00103
3	0.031	0.00185 ± 0.00106
4	0.047	0.00246 ± 0.00139
5	0.069	0.00263 ± 0.00145
6	0.101	0.00296 ± 0.00148
7	0.145	0.00527 ± 0.00148
8	0.207	0.00763 ± 0.00191
9	0.269	0.01024 ± 0.00166
10	0.421	0.01722 ± 0.00189
11	0.599	0.02219 ± 0.002046
12	0.849	0.03240 ± 0.00292
13	1.104	0.04580 ± 0.00500
14	1.704	0.06658 ± 0.00854

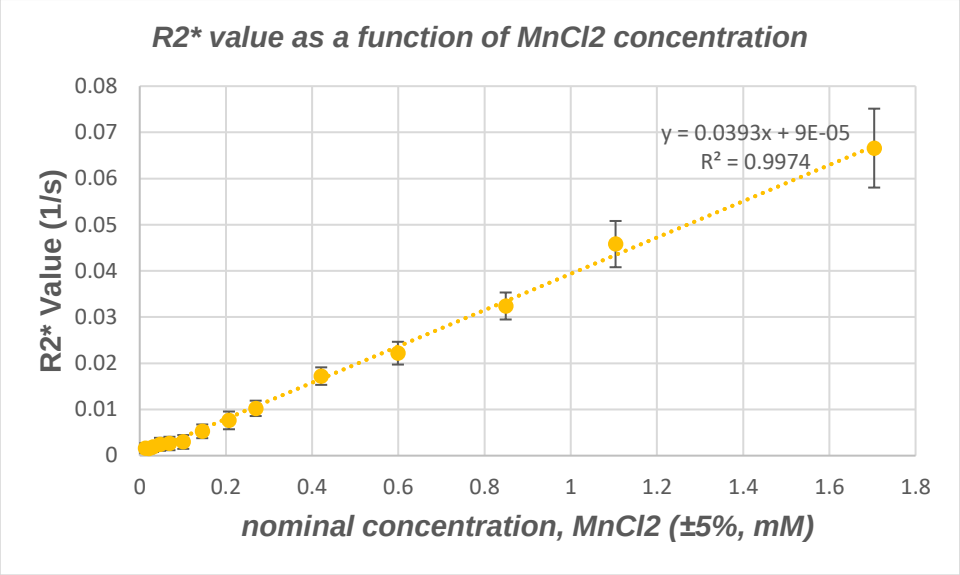

Figure 27. Measured $R2^*$ value from STAGE acquired by averaging of six intra session acquisitions as a function of nominal $MnCl_2$ concentration. The linear relationship indicates that the relative $R2^*$ map is justified.

Table 8. STAGE R2 map value acquired by averaging of five inter session acquisitions, for all spheres in T2 array for inter-sessions. The sphere nominal MnCl2 concentration is considered as a reference for validation.*

Spheres	$MnCl_2$ Concentration (±5%, mM)	STAGE R_2^* (1/s)
1	0.013	0.00164 ± 0.00109
2	0.021	0.00173 ± 0.00122
3	0.031	0.00167 ± 0.00104
4	0.047	0.00246 ± 0.00128
5	0.069	0.00248 ± 0.00128
6	0.101	0.00357 ± 0.00144
7	0.145	0.00546 ± 0.00148
8	0.207	0.00745 ± 0.00135
9	0.269	0.01013 ± 0.00132
10	0.421	0.01649 ± 0.00118
11	0.599	0.02216 ± 0.00158
12	0.849	0.03270 ± 0.00220
13	1.104	0.04508 ± 0.00327
14	1.704	0.06767 ± 0.00664

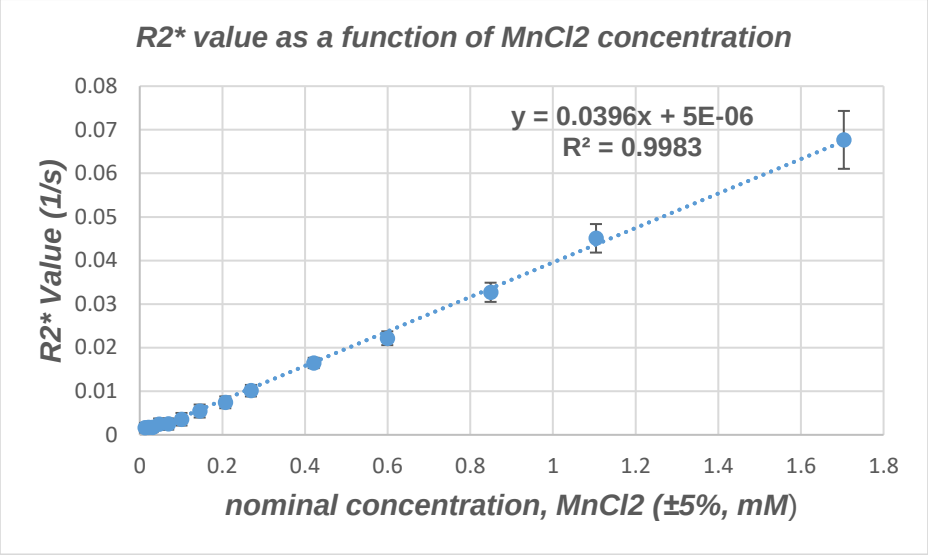

Figure 28. Measured R2 value from STAGE acquired by averaging of five inter session acquisitions, as a function of nominal MnCl2 concentration. The linear relationship indicates that the relative R2* map is justified.*

.

Chapter References

Chen, X., & Qiu, B. (2018). A pilot study of short T2* measurements with ultrashort echo time imaging at 0.35 T. *BioMedical Engineering Online*, *17*(1), 1–8. https://doi.org/10.1186/s12938-018-0505-5

Keenan, K., Boos, M., Jackson, E. F., Kown, S.-J., Jennings, D., & Russek, S. (2013). NIST/ISMRM MRI System Phantom T1 Measurements on Multiple MRI System. *Proceedings 21st Scientific Meeting, International Society for Magnetic Resonance in Medicine*, *21*, 4338. Retrieved from http://collaborate.nist.gov/mriphantoms/bin/view/MriPhantoms/

Keenan, K. E., Stupic, K. F., Boss, M. A., Russek, S. E., Chenevert, T. L., Prasad, P., … Jackson, E. (2016). Comparison of T1 measurement using ISMRM / NIST phantom comparison of T1 measurement using ISMRM / NIST system phantom. *ISMRM 24th Annual Meeting, Singapore, 2016.*

Maubon, A. J., Ferru, J. M., Berger, V., Soulage, M. C., DeGraef, M., Aubas, P., … Rouanet, J. P. (1999). Effect of field strength on MR images: comparison of the same subject at 0.5, 1.0, and 1.5 T. *Radiographics : A Review Publication of the Radiological Society of North America, Inc*, *19*(4), 1057–1067. https://doi.org/10.1148/radiographics.19.4.g99jl281057

Russek SE, Boss M, Jackson EF, Jennings DL, Evelhoch JL, G. J., & AG, S. (2012). Characterization of NIST/ISMRM MRI System Ph hantom. *Characterization of NIST/ISMRM MRI System Phantom. In Proceedings of the 20th Annual Meeting of ISMRM, Melbourne, Australia*, *20*, 2456. Retrieved from http://archive.ismrm.org/2012/2456.html

Tofts, P. (2014). Quantitative MRI of the brain: measuring changes caused by disease. *2003 John Wiley & Sons, Ltd*, *78*(925), 87–87. https://doi.org/10.1259/bjr.78.925.780087a

Chapter 5

Conclusion

Conclusion

Optimum magnetic field strength is an argument that has been debated over the past two decades in the field of MRI research. High magnetic field provides higher SNR, higher resolution, faster imaging, better temporal contrast in functional MRI, more capabilities in MR spectroscopy, etc. However, there are some advantages of low field MRI that no one can deny (Ladd et al., 2018).

Susceptibility artifacts usually occur at the interface of two tissues with huge susceptibility differences. This results in magnetic field perturbation and image distortion in the mentioned boundaries. Since this kind of artifact is recognized as delicate, it may mislead physicians and create false detection. Paranasal sinuses and bone-soft tissue interfaces are c regions where susceptibility artifacts commonly occur. Chemical shift artifacts are another kind of artifact that can arise in the boundaries with large susceptibility differences on the sides. Both artifacts escalate at high field and minimize at low field.

An open controversial issue is limitation of higher radio frequency pulses in MR imaging. As the magnetic field is increased, the RF power depositions also increase, which results in decreasing RF penetration depth in biological tissues. Previously, it has been shown that for homogeneous cylinders with isotropic electrical conductivity, there is relation of a fourth power dependence of absorbed RF power deposition with average body size (Bottomley & Andrew, 1978).

This work highlights the potential for using STAGE to acquire serial data for patients undergoing daily MRgRT for cancer radiation therapy. These data may yield quantitative metrics to monitor tumors, normal tissue, and post-surgical changes at low magnetic field strengths even without dedicated head coils. While low-field strengths may be known for their low SNR, they also offer the advantages of reduced susceptibility, chemical shift, and geometric distortion artifacts.

We have successfully translated STAGE to a low field strength MR-linac to yield 4 qualitative multi-contrast and 4 quantitative multi-parametric images, in under 10 minutes.

Future perspective

We introduced a variety of new contrasts for this type of low field scanning by using STAGE imaging. Integrating STAGE quantitative maps with bSSFP resulted in a quantitative T2 map which can help to visualize the tumor and its boundaries.

As described, STAGE consists of two triple spoiled gradient sequence. The phase information in this sequence is proportional to the product of magnetic field variation and echo time. For a right-hand system, the phase is given by (Brown, Cheng, & Haacke, 2014):

$$\varphi = \gamma * \Delta B * TE + \varphi_0 \tag{5.1}$$

Where φ_0 is the phase offset at TE is zero, and it depends on the hardware. The φ_0 can be found by complex division of the second echo to the first echo if the second echo time is twice the first one. Then φ_0 term should be subtracted from the original phase images. (subtract here means complex division). The relationship between phase information and resonance offset (β) is characterized as:

$$\begin{cases} \varphi - \varphi_0 = \int_0^{TE} \omega(t)dt = \int_0^{TE} \gamma B(t)dt = \gamma \Delta B * TE \\ \beta = \int_0^{TR} \omega(t)dt = \int_0^{TR} \gamma B(t)dt = \gamma \Delta B * TR \end{cases} \tag{5.2}$$

$$\Rightarrow \beta = (\varphi - \varphi_0) * \frac{T_R}{T_E} \tag{5.3}$$

It can be shown that the bSSFP signal is given by

$$bSSFP = \frac{M_0(1 - E_1)\sin\theta\sqrt{1 - 2E_2\cos\beta + E_2^2}}{(1 - E_1\cos\theta - E_2^2E_1 + E_2^2\cos\theta) + \cos\beta\,((E_1 - \cos\theta)E_2 - E_2(1 - E_1\cos\theta)} \tag{5.4}$$

where M_0 represents the PD, θ is the flip angle (FA), β is the off-resonance term, $E_1 = \exp(-\frac{TR}{T1})$ and $E_2 = \exp\left(-\frac{TR}{T2}\right)$.

In order to find T2 from a single scan, $M_0, T1$ and β are required. The first two parameters can be obtained from STAGE data and β based on equation (5.3). A straight-forward solution to find E2 (and T2) is dividing two bSSFP signals together in two days.

1- Dividing one bSSFP signal with a contenious RF pulse in the same direction $(\theta, \theta, \dots)$ to an alternating RF pulse $(-\theta, \theta, \dots)$
2- Dividing two bSSFP signal together either with RF pulse in the same direction or alternating RF pulse

Assume that a signal from the RF pulse is in the same direction denoted by S_1 and the signal from the alternating RF pulse is denoted by S_2

$$S_1 = \frac{M_0(1-E_1)\sin\theta\sqrt{1-2E_2\cos\beta+E_2^2}}{(1-E_1\cos\theta-E_2^2E_1+E_2^2\cos\theta)+\cos\beta\,((E_1-\cos\theta)E_2-E_2(1-E_1\cos\theta))} \quad (5.5)$$

In alternating RF pulse sequence beta will be shifted by π and since $\cos(\beta+\pi) = -\cos\beta$

$$S_2 = \frac{M_0(1-E_1)\sin\theta\sqrt{1-2E_2\cos(\beta+\pi)+E_2^2}}{(1-E_1\cos\theta-E_2^2E_1+E_2^2\cos\theta)+\cos(\beta+\pi)\,((E_1-\cos\theta)E_2-E_2(1-E_1\cos\theta))}$$

$$\Rightarrow$$

$$S_2 = \frac{M_0(1-E_1)\sin\theta\sqrt{1+2E_2\cos(\beta)+E_2^2}}{(1-E_1\cos\theta-E_2^2E_1+E_2^2\cos\theta)-\cos(\beta)\,((E_1-\cos\theta)E_2-E_2(1-E_1\cos\theta))} \quad (5.6)$$

Let divide the signals:

$$\frac{S_1}{S_2} = \frac{\frac{\sqrt{1-2E_2\cos\beta+E_2^2}}{(1-E_1\cos\theta-E_2^2E_1+E_2^2\cos\theta)+\cos\beta\,((E_1-\cos\theta)E_2-E_2(1-E_1\cos\theta))}}{\frac{\sqrt{1+2E_2\cos\beta+E_2^2}}{(1-E_1\cos\theta-E_2^2E_1+E_2^2\cos\theta)-\cos(\beta)\,((E_1-\cos\theta)E_2-E_2(1-E_1\cos\theta))}} \quad (5.7)$$

So E2 (also T2) can be find through a quadratic equation.

Another approach is dividing two bSSFP signals either with RF pulse in the same direction or alternating the RF pulse

$$S_1 = \frac{M_0(1-E_1)\sin\theta_1\sqrt{1-2E_2\cos\beta+E_2^2}}{(1-E_1\cos\theta_1-E_2^2E_1+E_2^2\cos\theta_1)+\cos\beta\,((E_1-\cos\theta_1)E_2-E_2(1-E_1\cos\theta_1))} \quad (5.8)$$

$$S_2 = \frac{M_0(1-E_1)\sin\theta_2\sqrt{1-2E_2\cos\beta+E_2^2}}{(1-E_1\cos\theta_2-E_2^2E_1+E_2^2\cos\theta_2)+\cos\beta\,((E_1-\cos\theta_2)E_2-E_2(1-E_1\cos\theta_2))} \quad (5.9)$$

$$\frac{S_1}{S_2} = \frac{\frac{\sin\theta_1}{(1-E_1\cos\theta_1-E_2^2E_1+E_2^2\cos\theta_1)+\cos\beta\,((E_1-\cos\theta_1)E_2-E_2(1-E_1\cos\theta_1))}}{\frac{\sin\theta_2}{(1-E_1\cos\theta_2-E_2^2E_1+E_2^2\cos\theta_2)+\cos\beta\,((E_1-\cos\theta_2)E_2-E_2(1-E_1\cos\theta_2))}} \quad (5.10)$$

And E2 (also T2) is accessible. A self-consistent solution is similarity of all output of suggested ways.

Chapter References

Bottomley, P. A., & Andrew, E. R. (1978). RF magnetic field penetration, phase shift and power dissipation in biological tissue: implications for NMR imaging. *Physics in Medicine and Biology*, *23*(4), 630–643.

Brown, R., Cheng, Y., & Haacke, E. (2014). *Magnetic Resonance Imaging: Physical Properties and Sequence Design* (2nd Editio). Retrieved from https://onlinelibrary.wiley.com/doi/book/10.1002/9781118633953

Ladd, M. E., Bachert, P., Meyerspeer, M., Moser, E., Nagel, A. M., Norris, D. G., … Zaiss, M. (2018). Pros and cons of ultra-high-field MRI/MRS for human application. *Progress in Nuclear Magnetic Resonance Spectroscopy*, *109*, 1–50. https://doi.org/https://doi.org/10.1016/j.pnmrs.2018.06.001